Chapter 11
Discrete Description of Crack Kinematics in Regularized Free Discontinuities of Crack Faces

Bo Yin, Johannes Storm, and Michael Kaliske

Abstract The fracture mechanical free discontinuity problem can be associated with a generalized, variational approach of GRIFFITH's fracture theory. By introducing a regularization for the sharp displacement discontinuity at cracks and crack surfaces, stable computational fracture models are developed, e.g., the phase-field fracture formulation and the eigenfracture approach. The presented work summarizes recent findings regarding unrealistic deformation kinematics at cracks predicted by conventional formulations of both models and introduces the variational framework of *Representative Crack Element* to overcome these discrepancies. Illustrative examples for crack propagation and post-fracture behavior at small and finite deformations, brittle and cohesive failure as well as for rate-dependent materials frictional crack contact demonstrate the flexibility and the generality of of the introduced *Representative Crack Element*.

Key words: Free discontinuity, Eigenfracture, Phase-field fracture, Representative crack element

11.1 Introduction

The research on material failure, including strain softening, brittle rupture, cohesive delamination, and fatigue aging, is becoming an area of increasing interest in engineering application. A number of failure mechanisms is identified and a variety of criteria are postulated to effectively predict material strength within a safe and controllable application. To provide a reliable prediction, crack initiation, propagation, kinking, and branching studies are of importance and necessity. Meanwhile, crack deformation kinematics during fracture evolution plays an equivalent role as afore-

Bo Yin · Johannes Storm · Michael Kaliske
Institute for Structural Analysis, TU Dresden, 01062 Dresden, Germany,
e-mail: bo.yin@tu-dresden.de, johannes.storm@tu-dresden.de, michael.kaliske@tu-dresden.de

H. Altenbach et al. (eds.), *Material Modeling and Structural Mechanics*,
Advanced Structured Materials 161, https://doi.org/10.1007/978-3-030-97675-0_11

mentioned features during fracture evolution. Taking a closing crack deformation as one representative example, material integrity is preserved and loading normal to the crack surfaces can be fully transferred from one side to the other one through the crack surfaces. Furthermore, a relative motion of the two contacted crack faces may yield other mechanical phenomena, e.g., friction, abrasion and corrosion, which are realistically and physically featured in particular for complex and mixed load patterns. Originally inspired by experimental investigations, Griffith (1921) proposed a conceptual understanding of brittle crack formation, namely, the energetic balance between the stored strain potential and the crack forming dissipation. To depict the amount of strain energy consumed to generate a unit crack surface during fracture evolution, an important material parameter is defined, $\mathcal{G}_c$, known as the critical energy release rate or the fracture toughness. The triggering condition of fracture evolution is that the instantaneous energy $\mathcal{G}$ reaches or exceeds the critical value, i.e., $\mathcal{G} \geqslant \mathcal{G}_c$. This classical GRIFFITH fracture theory provides a physical understanding of crack nucleation and propagation criterion, but unfortunately, does not provide an explicit definition for the crack propagation path during fracture evolution.

In the past decades, a variety of numerical methods has been developed to model reliably fracture evolution. By categorizing the present models, crack approximation is numerically described by either a discrete or a continuous, smeared approach. Regarding the former one, a discrete crack methodology renders, e.g., the crack boundary as an explicit element edge within the finite element discretization. The crack-induced displacement discontinuity is, hence, naturally modeled based on the geometrical boundary. Material separation due to the existence of cracks is straightforwardly modeled for an opening or shearing crack deformation. Nevertheless, numerical complexity arises for a closing crack deformation with respect to crack surface interpenetration. To address crack contact, additional algorithmic efforts are required. The classical cohesive zone model (Barenblatt, 1962; Dugdale, 1960; Schellekens and de Borst, 1993; Alfano and Crisfield, 2001; Foulk et al., 2000; Ortiz and Pandolfi, 1999) is a representative approach of discrete crack approximation, which constitutes the traction-separation relationship based on the crack opening distance. It is intensively applied to pre-known crack path problems, unfortunately, the prediction of an unknown crack propagation largely increases computational efforts. Another concept, the configurational force method (Gurtin, 2000; Kienzler and Herrmann, 2000; Maugin, 1995; Braun, 1997; Maugin, 2010; Miehe and Gürses, 2007; Mueller and Maugin, 2002), is frequently applied to discrete crack approaches, which depicts a non-NEWTONIAN force acting on a crack tip within a homogeneous domain. The calculated material force allows for a prediction of crack growth direction and provides a crack evolving criterion. Thereafter, several approaches adopt a node splitting algorithm and an r-adaptivity re-meshing strategy to model crack propagation. Nevertheless, these methodologies are restricted by the fact that an initial notch is required to generate stress concentrations.

De Giorgi and Ambrosio (1988) have provided a general variational description through the formulation of free discontinuity problems. In general, unknown field variables are allowed to have jumps, meanwhile, the locations of the discontinuities are unknown. The existence of minimizers is successfully shown in the space of

special functions of bounded variation, see Ambrosio et al. (2000) for an overview. Although used in other contexts, free discontinuity problems can be interpreted as a generalization of GRIFFITH's criterion. However, computational solutions of free discontinuity problems are difficult and have lead to several regularized formulations, e.g., phase-field fracture and eigenfracture to name two representatives in the context of fracture mechanics. Closed form proofs exist for both methods, where the regularized models converge to the original free discontinuity problem for decreasing regularization lengths and discretization sizes, see e.g. Ambrosio and Tortorelli (1990) and Schmidt et al. (2009).

With respect to smeared crack approximation, the phase-field approach for fracture depicts a continuous and diffusive crack representation from the numerical point of view. Incorporating classical GRIFFITH's fracture theory, Francfort and Marigo (1998) formulates a brittle fracture model by thermodynamically minimizing the internal strain energy potential and the fracture energy, see also Bourdin et al. (2000, 2008); Hakim and Karma (2009); Miehe et al. (2010b); Pham et al. (2011) for detailed insights. Thereafter, several publications, e.g., Borden et al. (2014); Linse et al. (2017); Chambolle et al. (2018), study classical Γ-convergence for phase-field modeling in the field of fracture evolution. Furthermore, brittle phase-field modeling is subsequently extended to different features, e.g., rate-dependent fracture (Yin et al., 2020b; Yin and Kaliske, 2020c; Shen et al., 2019; Schänzel, 2015; Loew et al., 2019), ductile fracture (Ambati et al., 2015a; Miehe et al., 2015; Borden et al., 2016; Yin and Kaliske, 2020b), anisotropic fracture (Gültekin et al., 2018; Teichtmeister et al., 2017; Yin and Kaliske, 2020a), cohesive fracture (Verhoosel and de Borst, 2013; Vignollet et al., 2014; Nguyen and Wu, 2018; Geelen et al., 2019), and fatigue fracture (Alessi et al., 2018; Carrara et al., 2020; Seiler et al., 2020; Yin et al., 2020a), to name a few.

The much younger eigenfracture method is developed by Schmidt et al. (2009) and is applied to problems of linear elasticity and elasto-plasticity, see for instance Pandolfi and Ortiz (2012); Stochino et al. (2017); Qinami et al. (2020) for some early applications. Similar to phase-field fracture, a second field is introduced called eigenstrain in order to relax the sharp displacement jump at the crack. However, the second field is solved at the material level and equivalently the crack evolution in a post-processing step after each load step of the mechanical problem. Less degrees of freedom and a better convergence behavior yield relatively low computational costs compared to phase-field fracture. Pandolfi et al. (2021) have further demonstrated a larger Γ-convergence rate for eigenfracture versus phase-field fracture, which allows to obtain the same solution accuracy like for phase-field fracture on coarser meshes. On the other side, the eigenfracture method is still in an early development stage and further studies on the properties of the method are necessary.

The strength of the phase-field fracture and the eigenfracture method is the capability to capture crack initiation and propagation with complex patterns independent of any specific criterion. Nevertheless, one of the challenging tasks is prediction of the deformation kinematics of crack surfaces under complex loading states, e.g., opening, closing, shearing and mixed mode. A realistic determination of the material stiffness degradation considering complex crack deformation kinematics

is significantly important. In many publications, sophisticated approaches are proposed to approximate the correct crack kinematics by decompositions of the strain energy potential. A comprehensive review of existing split models can be found in Ambati et al. (2015b); Storm et al. (2020). As one common choice based upon a straightforward volumetric and deviatoric energetic decomposition, Amor et al. (2009) and Freddi and Royer-Carfagni (2009) propose the fracture driving force for volume shrinkage by excluding the volumetric energy contribution. Another commonly used split, postulated by Miehe et al. (2010a), is depending upon a spectral decomposition scheme. The strain tensor is decomposed into the eigenvalues and the elastic strain energy density is redefined by using the tensile and compressive strain components. For other representative split models, it is referred to e.g. Henry and Levine (2004); Lancioni and Royer-Carfagni (2009); Freddi and Royer-Carfagni (2010); Hesch and Weinberg (2014). Nevertheless, these models cannot yield physical crack deformations under complex loading conditions. Thereafter, several attempts are proposed to address this issue. A conceptual *Directional Decomposition* is considered by Strobl and Seelig (2016); Steinke and Kaliske (2019); Luo et al. (2021) to reformulate the strain or stress quantity by taking the local crack orientation into consideration. As a result, these models successfully address the issue of crack kinematics compared to the aforementioned V-D split and spectral split approaches. Nevertheless, the approaches are unfortunately restricted to an isotropic, linear elastic solid at small strain. The basis of the *Directional Decomposition* is formed by the local crack orientation. Applying the concept of maximum dissipation, the crack orientation can be formulated as a variational problem (Bryant and Sun, 2018). However, this minimization is non-convex and computationally hard to solve without further restrictions. Therefore, several approximation are proposed to capture crack orientation, e.g. the gradient of the phase-field (Strobl and Seelig, 2016) and the maximum principal stress direction (Steinke and Kaliske, 2019).

With the intention to generalize the *Directional Decomposition* model and to overcome its limitations, the framework of *Representative Crack Elements (RCE)* is developed. On the basis of variational homogenization theory (Blanco et al., 2016), Storm et al. (2020) introduce the fundamental theory which allows to consistently derive realistic crack kinematics from representative discrete crack models and to transfer the overall behavior to the regularized crack models. The RCE concept is first applied to bulk materials considering anisotropic elasticity and thermoelasticity in the context of phase-field fracture. Subsequently, applications to viscoelasticity (Yin et al., 2021), crack face friction, inelastic materials and finite deformations, fully coupled thermo-mechanics (Storm et al., 2021b), cohesive fracture and eigenfracture (Storm et al., 2021a) are developed. Within the work at hand, a review of the RCE framework applied to phase-field fracture and to eigenfracture in the context of the regularized free discontinuity problem is presented. In particular, a fundamental theoretical background of the RCE framework is provided, which includes the strain kinematics for both the continuous and the RCE description. A virtual power principle is employed within the RCE to solve the unknown crack deformations within the RCE. In the sequel, the phase-field fracture and the eigenfracture modeling within an RCE framework are briefly summarized. Several

representative numerical examples have been presented to show the general applicability of the conceptual RCE modeling.

11.2 Representative Crack Elements

11.2.1 Structure and Notation

The classical *Representative Volume Element* concept bases upon the theory of homogenization. It is referred to Blanco et al. (2016) for a general summary. The principle of multi-scale virtual power, which is based on the first thermodynamical theorem, provides the theoretical foundation of homogenization theory. Meanwhile, this principle is a generalization of the HILL-MANDEL condition of stress work conservation (Hill, 1963). The work at hand adopts a similar methodology to formulate the so-called *Representative Crack Element (RCE)* framework, which on purpose incorporates a regularized approach to resolve the issues of accurate deformations kinematics in free discontinuity problems, see phase-field fracture modeling (Storm et al., 2020) and eigenfracture modeling (Storm et al., 2021a).

The fundamental derivation and illustration start from a definition of the basic notational description. Two classes of mathematical fonts, namely, a standard one and a fraktur one, are used to depict the quantities of the regularized fracture model and of the RCE model, respectively. Explicitly, the symbols

$$\mathfrak{G}\big|_{\mathfrak{x}} = \nabla_{\mathfrak{x}}\mathfrak{u} \qquad \text{and} \qquad \mathsf{G}\big|_{\mathsf{x}} = \nabla_{\mathsf{x}}\mathfrak{u} \tag{11.1}$$

are the general spatial gradient terms of $\mathfrak{u}$ and $\mathfrak{u}$ with respect to the RCE and the continuous descriptions, respectively. A schematic depiction of an RCE motion is shown in **Fig. 11.1** including the reference and deformed RCE blocks. The crack

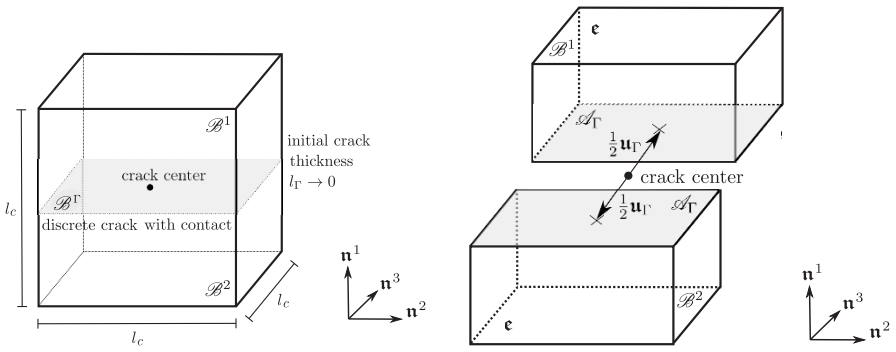

(a) discrete crack in RCE (b) crack opening in RCE

Fig. 11.1: Schematic description of crack kinematics of the RCE approach.

displacement in the RCE is denoted as

$$\mathbf{u}_\Gamma = \sum_{\mathrm{I}=1}^{3} u_\Gamma^{\mathrm{I}} \mathbf{n}^{\mathrm{I}}, \tag{11.2}$$

where the normal and tangential unit vectors with respect to the crack surface are expressed by $\mathbf{n}^1$ and $\mathbf{n}^{2,3}$, respectively. Two important conditions

- linear boundary constraints of upper and lower block surfaces in respective $\mathcal{B}^1$ and $\mathcal{B}^2$,
- identical and homogeneous deformations of upper and lower blocks in respective $\mathcal{B}^1$ and $\mathcal{B}^2$, and also homogeneous crack deformation in $\mathcal{B}^\Gamma$

provide basic assumptions for the understanding and the derivation of the kinematics in an RCE. The dimensional length of the RCE is given as $\mathrm{l_c}$ and the two identical solid blocks ($\mathcal{B}^1$ for the upper one and $\mathcal{B}^2$ for the lower one) have the volumes $\mathcal{V}^1 = \mathcal{V}^2 = \mathrm{l_c^3}/2$. In addition to the two solid subdomains $\mathcal{B}^1, \mathcal{B}^2$, another subdomain is characterized by the crack space $\mathcal{B}^\Gamma$, where the infinitesimal thickness of the crack space is assumed to be $\mathrm{l}_\Gamma \to 0$. Hence, the cross-sectional area and the volume of the crack subdomain are approximated by $\mathcal{A}_\Gamma = \mathrm{l_c^2}$ and $\mathcal{V}^\Gamma = \mathcal{A}_\Gamma \mathrm{l}_\Gamma = \mathrm{l_c^2}\,\mathrm{l}_\Gamma$, respectively. The total domain is expressed as $\mathcal{B} = \mathcal{B}^1 \cup \mathcal{B}^2 \cup \mathcal{B}^\Gamma$, and the entire volume of an RCE is $\mathcal{V} = \mathcal{V}^1 + \mathcal{V}^2 + \mathcal{V}^\Gamma$.

11.2.2 Kinematic Coupling

The fundamental coupling relation of the regularized fracture model and the RCE reads

$$\mathbf{u} = \mathbf{u} + \mathbf{G}\big|_{\mathbf{x}} \cdot \left(\mathfrak{X} - \hat{\mathfrak{X}}^{\mathrm{ref}}\right) + \tilde{\mathbf{u}}. \tag{11.3}$$

Considering the homogeneous deformation fields at the RCE, the displacement fields at the three subdomains are given by

$$\mathbf{u} = \begin{cases} \hat{\mathbf{u}}^1 + \mathfrak{G}_{\mathrm{b}}\big|_{\mathfrak{X}} \cdot \left(\mathfrak{X} - \hat{\mathfrak{X}}^{\mathrm{ref}}\right) = \hat{\mathbf{u}}^1 + \left(\mathbf{G}\big|_{\mathbf{x}} + \tilde{\mathfrak{G}}_{\mathrm{b}}\big|_{\mathfrak{X}}\right) \cdot \left(\mathfrak{X} - \hat{\mathfrak{X}}^{\mathrm{ref}}\right), & \forall \mathfrak{X} \in \mathcal{B}^1, \\ \hat{\mathbf{u}}^2 + \mathfrak{G}_{\mathrm{b}}\big|_{\mathfrak{X}} \cdot \left(\mathfrak{X} - \hat{\mathfrak{X}}^{\mathrm{ref}}\right) = \hat{\mathbf{u}}^2 + \left(\mathbf{G}\big|_{\mathbf{x}} + \tilde{\mathfrak{G}}_{\mathrm{b}}\big|_{\mathfrak{X}}\right) \cdot \left(\mathfrak{X} - \hat{\mathfrak{X}}^{\mathrm{ref}}\right), & \forall \mathfrak{X} \in \mathcal{B}^2, \\ \hat{\mathbf{u}}_\Gamma + \mathfrak{G}_\Gamma\big|_{\mathfrak{X}} \cdot \left(\mathfrak{X} - \hat{\mathfrak{X}}^{\mathrm{ref}}\right) = \hat{\mathbf{u}}_\Gamma + \left(\mathbf{G}\big|_{\mathbf{x}} + \tilde{\mathfrak{G}}_\Gamma\big|_{\mathfrak{X}}\right) \cdot \left(\mathfrak{X} - \hat{\mathfrak{X}}^{\mathrm{ref}}\right), & \forall \mathfrak{X} \in \mathcal{B}^\Gamma, \end{cases} \tag{11.4}$$

where the quantities $\hat{\mathbf{u}}^1$, $\hat{\mathbf{u}}^2$ and $\hat{\mathbf{u}}_\Gamma$ are the rigid body translations of the three subdomains. The reference coordinate is

$$\hat{\mathfrak{X}}^{\mathrm{ref}} = \frac{1}{\mathcal{V}} \int_{\mathcal{B}} \mathfrak{X} \, \mathrm{d}\mathcal{V}. \tag{11.5}$$

Thereafter, decomposing the RCE into three subdomains, the RCE displacements and gradients vary with respect to each other. The second assumption aforementioned characterizes the identical RCE displacement gradient $\mathfrak{G}_{\mathrm{b}}\big|_{\mathfrak{X}}$ for the upper and lower block, reading

$$\mathfrak{G}_{\mathrm{b}}\big|_{\mathfrak{X}} = \mathbf{G}\big|_{\mathbf{x}} + \tilde{\mathfrak{G}}_{\mathrm{b}}\big|_{\mathfrak{X}} \qquad \forall \mathfrak{X} \in \left(\mathcal{B}^1 \cup \mathcal{B}^2\right), \tag{11.6}$$

where the gradient fluctuation in the subdomains of solid blocks is described by $\tilde{\mathfrak{G}}_{\mathrm{b}}\big|_{\mathfrak{X}}$. Similarly, the RCE gradient in the crack subdomain $\mathfrak{G}_{\Gamma}\big|_{\mathfrak{X}}$ reads

$$\mathfrak{G}_{\Gamma}\big|_{\mathfrak{X}} = \mathbf{G}\big|_{\mathbf{x}} + \tilde{\mathfrak{G}}_{\Gamma}\big|_{\mathfrak{X}} \qquad \forall \mathfrak{X} \in \mathcal{B}^{\Gamma}, \tag{11.7}$$

where the gradient fluctuation in the crack subdomain is denoted by $\tilde{\mathfrak{G}}_{\Gamma}\big|_{\mathfrak{X}}$. Hence, a general relation in the RCE is defined as

$$\mathfrak{G}\big|_{\mathfrak{X}} = \mathbf{G}\big|_{\mathbf{x}} + \tilde{\mathfrak{G}}\big|_{\mathfrak{X}}, \qquad \text{where} \qquad \tilde{\mathfrak{G}}\big|_{\mathfrak{X}} = \begin{cases} \tilde{\mathfrak{G}}_{\mathrm{b}}\big|_{\mathfrak{X}}, & \forall \mathfrak{X} \in \left(\mathcal{B}^1 \cup \mathcal{B}^2\right), \\ \tilde{\mathfrak{G}}_{\Gamma}\big|_{\mathfrak{X}}, & \forall \mathfrak{X} \in \mathcal{B}^{\Gamma}. \end{cases} \tag{11.8}$$

According to the evaluation of the compatibility condition for kinematically admissible displacement fluctuations, the relations

$$\mathbf{u} = \frac{1}{\mathcal{V}} \int_{\mathcal{B}} \mathbf{u} \, \mathrm{d}\mathcal{V} \qquad \text{and} \qquad \mathbf{0} = \frac{1}{\mathcal{V}} \int_{\mathcal{B}} \tilde{\mathbf{u}} \, \mathrm{d}\mathcal{V} \tag{11.9}$$

and

$$\mathbf{G}\big|_{\mathbf{x}} = \frac{1}{\mathcal{V}} \int_{\mathcal{B}} \mathfrak{G}\big|_{\mathfrak{X}} \, \mathrm{d}\mathcal{V} \qquad \text{and} \qquad \mathbf{0} = \frac{1}{\mathcal{V}} \int_{\mathcal{B}} \tilde{\mathfrak{G}}\big|_{\mathfrak{X}} \, \mathrm{d}\mathcal{V} \tag{11.10}$$

exist, where the terms $\tilde{\mathbf{u}}$ and $\tilde{\mathfrak{G}}\big|_{\mathfrak{X}}$ represent the displacement and the gradient fluctuations with respect to the RCE description in a general case. Furthermore, one obtains a symmetric rigid body translations of both, the upper and lower block, with respect to the crack center displacement at continuous level $\mathbf{u}$, reading

$$\hat{\mathbf{u}}^1 = \mathbf{u} + \frac{1}{2}\mathbf{u}_{\Gamma}, \qquad \hat{\mathbf{u}}^2 = \mathbf{u} - \frac{1}{2}\mathbf{u}_{\Gamma}, \qquad \hat{\mathbf{u}}_{\Gamma} = \mathbf{u}. \tag{11.11}$$

As a result, the displacement fluctuations eventually are obtained as

$$\tilde{\mathbf{u}} = \begin{cases} \frac{1}{2}\mathbf{u}_{\Gamma} + \left(\mathbf{G}\big|_{\mathbf{x}} + \tilde{\mathfrak{G}}_{\mathrm{b}}\big|_{\mathfrak{X}}\right) \cdot \left(\mathfrak{X} - \hat{\mathfrak{X}}^{\mathrm{ref}}\right), & \forall \mathfrak{X} \in \mathcal{B}^1, \\ -\frac{1}{2}\mathbf{u}_{\Gamma} + \left(\mathbf{G}\big|_{\mathbf{x}} + \tilde{\mathfrak{G}}_{\mathrm{b}}\big|_{\mathfrak{X}}\right) \cdot \left(\mathfrak{X} - \hat{\mathfrak{X}}^{\mathrm{ref}}\right), & \forall \mathfrak{X} \in \mathcal{B}^2, \\ \left(\mathbf{G}\big|_{\mathbf{x}} + \tilde{\mathfrak{G}}_{\Gamma}\big|_{\mathfrak{X}}\right) \cdot \left(\mathfrak{X} - \hat{\mathfrak{X}}^{\mathrm{ref}}\right), & \forall \mathfrak{X} \in \mathcal{B}^{\Gamma}. \end{cases} \tag{11.12}$$

The projection of the crack deformation normal to the crack surface in the RCE is

$$\tilde{\mathfrak{G}}_{\Gamma}\big|_{\mathfrak{X}} \cdot \mathbf{n}^1 = \frac{\mathbf{u}_{\Gamma}}{l_{\Gamma}} = \sum_{I=1}^{3} \frac{u_{\Gamma}^{I}}{l_{\Gamma}} \mathbf{n}^I \qquad \forall \mathfrak{X} \in \mathcal{B}^{\Gamma}, \tag{11.13}$$

which further leads to the crack deformation gradient as

$$\tilde{\mathfrak{G}}_{\Gamma}\big|_{\mathfrak{X}} = \frac{\mathbf{u}_{\Gamma}}{l_{\Gamma}} \otimes \mathbf{n}^1 = \sum_{I=1}^{3} \frac{u_{\Gamma}^{I}}{l_{\Gamma}} \mathbf{n}^I \otimes \mathbf{n}^1 \qquad \forall \mathfrak{X} \in \mathcal{B}^{\Gamma}. \tag{11.14}$$

Considering kinematic coupling of gradient terms in Eq. $(11.10)_1$, the relation

$$\begin{aligned}
\mathsf{G}\big|_{\mathbf{x}} =& \frac{1}{\mathcal{V}} \left(\int_{\mathcal{B}^1 \cup \mathcal{B}^2} \mathfrak{G}_{\mathrm{b}}\big|_{\mathfrak{X}} \, \mathrm{d}\mathcal{V} + \int_{\mathcal{B}^{\Gamma}} \mathfrak{G}_{\Gamma}\big|_{\mathfrak{X}} \, \mathrm{d}\mathcal{V} \right) \\
=& \frac{1}{\mathcal{V}} \left(\int_{\mathcal{B}^1 \cup \mathcal{B}^2} \left(\mathsf{G}\big|_{\mathbf{x}} + \tilde{\mathfrak{G}}_{\mathrm{b}}\big|_{\mathfrak{X}} \right) \mathrm{d}\mathcal{V} + \int_{\mathcal{B}^{\Gamma}} \left(\mathsf{G}\big|_{\mathbf{x}} + \tilde{\mathfrak{G}}_{\Gamma}\big|_{\mathfrak{X}} \right) \mathrm{d}\mathcal{V} \right) \\
=& \frac{1}{\mathcal{V}} \Big(\left(\mathsf{G}\big|_{\mathbf{x}} + \tilde{\mathfrak{G}}_{\mathrm{b}}\big|_{\mathfrak{X}} \right) \left(\mathcal{V}^1 + \mathcal{V}^2 \right) + \left(\mathsf{G}\big|_{\mathbf{x}} + \tilde{\mathfrak{G}}_{\Gamma}\big|_{\mathfrak{X}} \right) \mathcal{V}^{\Gamma} \Big) \\
=& \frac{1}{\mathcal{V}} \Big(\mathsf{G}\big|_{\mathbf{x}} \mathcal{V} + \tilde{\mathfrak{G}}_{\mathrm{b}}\big|_{\mathfrak{X}} \left(\mathcal{V}^1 + \mathcal{V}^2 \right) + \tilde{\mathfrak{G}}_{\Gamma}\big|_{\mathfrak{X}} \mathcal{V}^{\Gamma} \Big) \\
=& \mathsf{G}\big|_{\mathbf{x}} + \frac{\tilde{\mathfrak{G}}_{\mathrm{b}}\big|_{\mathfrak{X}} \left(\mathcal{V}^1 + \mathcal{V}^2 \right) + \tilde{\mathfrak{G}}_{\Gamma}\big|_{\mathfrak{X}} \mathcal{V}^{\Gamma}}{\mathcal{V}}
\end{aligned} \tag{11.15}$$

exists, which forces the condition

$$\frac{\tilde{\mathfrak{G}}_{\mathrm{b}}\big|_{\mathfrak{X}} \left(\mathcal{V}^1 + \mathcal{V}^2 \right) + \tilde{\mathfrak{G}}_{\Gamma}\big|_{\mathfrak{X}} \mathcal{V}^{\Gamma}}{\mathcal{V}} = \mathbf{0}. \tag{11.16}$$

As a consequence, it subsequently leads to

$$\tilde{\mathfrak{G}}_{\mathrm{b}}\big|_{\mathfrak{X}} = -\frac{\mathcal{V}^{\Gamma}}{\mathcal{V}^1 + \mathcal{V}^2} \tilde{\mathfrak{G}}_{\Gamma}\big|_{\mathfrak{X}} = -\frac{l_{\mathrm{c}}^2 \, l_{\Gamma}}{l_{\mathrm{c}}^3} \tilde{\mathfrak{G}}_{\Gamma}\big|_{\mathfrak{X}} = -\frac{l_{\Gamma}}{l_{\mathrm{c}}} \sum_{I=1}^{3} \frac{u^I}{l_{\Gamma}} \mathbf{n}^I \otimes \mathbf{n}^1 = -\sum_{I=1}^{3} \frac{u^I}{l_{\mathrm{c}}} \mathbf{n}^I \otimes \mathbf{n}^1. \tag{11.17}$$

Meanwhile, the condition in Eq. (11.16) fulfills the second condition of the kinematically admissible displacement fluctuations in Eq. $(11.10)_2$, which can be interpreted as

$$\begin{aligned}
\mathbf{0} =& \frac{1}{\mathcal{V}} \int_{\mathcal{B}} \tilde{\mathfrak{G}}\big|_{\mathfrak{X}} \, \mathrm{d}\mathcal{V} = \frac{1}{\mathcal{V}} \left(\int_{\mathcal{B}^1 \cup \mathcal{B}^2} \tilde{\mathfrak{G}}_{\mathrm{b}}\big|_{\mathfrak{X}} \mathrm{d}\mathcal{V} + \int_{\mathcal{B}^{\Gamma}} \tilde{\mathfrak{G}}_{\Gamma}\big|_{\mathfrak{X}} \mathrm{d}\mathcal{V} \right) \\
=& \frac{\tilde{\mathfrak{G}}_{\mathrm{b}}\big|_{\mathfrak{X}} \left(\mathcal{V}^1 + \mathcal{V}^2 \right) + \tilde{\mathfrak{G}}_{\Gamma}\big|_{\mathfrak{X}} \mathcal{V}^{\Gamma}}{\mathcal{V}}.
\end{aligned} \tag{11.18}$$

Substituting the gradient fluctuation in Eq. (11.17) into Eq. (11.6), the RCE gradient of the block material of RCE reads

$$\mathfrak{G}_{\mathrm{b}}\big|_{\mathfrak{X}} = \mathsf{G}\big|_{\mathbf{x}} - \sum_{\mathrm{I}=1}^{3} \frac{\mathfrak{u}^{\mathrm{I}}}{\mathfrak{l}} \mathfrak{n}^{\mathrm{I}} \otimes \mathfrak{n}^{1} \qquad \forall \mathfrak{X} \in \left(\mathcal{B}^{1} \cup \mathcal{B}^{2}\right). \tag{11.19}$$

By further making use of the gradient terms, the second order strain tensors for both the continuous description and the RCE blocks are defined as

$$\boldsymbol{\varepsilon} = \frac{1}{2}\left(\mathsf{G}\big|_{\mathbf{x}} + \left(\mathsf{G}\big|_{\mathbf{x}}\right)^{\mathsf{T}}\right) \tag{11.20}$$

and

$$\mathfrak{e} = \frac{1}{2}\left(\mathfrak{G}_{\mathrm{b}}\big|_{\mathfrak{X}} + \left(\mathfrak{G}_{\mathrm{b}}\big|_{\mathfrak{X}}\right)^{\mathsf{T}}\right), \tag{11.21}$$

respectively. Substituting Eqs. (11.19) and (11.20) into Eq. (11.21), the relationship of the strain quantities between the continuous and the RCE description eventually yields

$$\mathfrak{e} = \boldsymbol{\varepsilon} - \sum_{\mathrm{I}=1}^{3} \Gamma^{\mathrm{I}} \mathfrak{P}^{\mathrm{I}}, \tag{11.22}$$

where

$$\Gamma^{\mathrm{I}} = \frac{\mathfrak{u}^{\mathrm{I}}}{\mathfrak{l}_{\mathrm{c}}} \qquad \text{and} \qquad \mathfrak{P}^{\mathrm{I}} = \frac{1}{2}\left(\mathfrak{n}^{\mathrm{I}} \otimes \mathfrak{n}^{1} + \mathfrak{n}^{1} \otimes \mathfrak{n}^{\mathrm{I}}\right). \tag{11.23}$$

Therefore, two important aspects, namely, the unknown crack orientation $\mathfrak{n}^{\mathrm{I}}$ and the unknown crack deformation Γ^{I} with $\mathrm{I} = 1,2,3$, need to be appropriately resolved to yield the consequent constitutive description of the RCE. The former one, the orientation of the orthogonal local RCE system $\mathcal{E}^{\Gamma} \sim \left\{\mathfrak{n}^{1}, \mathfrak{n}^{2}, \mathfrak{n}^{3}\right\}$ with respect to the global coordinate system $\mathcal{E}^{e} \sim \left\{\boldsymbol{e}^{1}, \boldsymbol{e}^{2}, \boldsymbol{e}^{3}\right\}$ is determined by an accurate crack orientation criterion, which is, nevertheless, still challenging for a robust definition of crack orientation. Herein, several simplified criteria or a predefined crack orientation can be considered with regard to this issue. Therefore, the only remaining issue is the solution for the crack deformation in the RCE framework.

11.2.3 Solution for the Crack Deformation in the RCE

The RCE block material is assumed to be characterized by the same constitutive law as the intact bulk material, whereas the local strain fields $\mathfrak{e}$ and $\boldsymbol{\varepsilon}$ are different. To describe the constitutive laws of the RCE and the intact material by a straightforward understanding, the HELMHOLTZ free energy functional is adopted to derive the stress and the consistent material tangent, reading

$$\mathfrak{s} = \frac{\partial \varphi(\mathfrak{e})}{\partial \mathfrak{e}}, \qquad \mathfrak{C} = \frac{\partial^2 \varphi(\mathfrak{e})}{\partial \mathfrak{e}^2}, \qquad \text{and} \qquad \boldsymbol{\sigma}^0 = \frac{\partial \varphi(\boldsymbol{\varepsilon})}{\partial \boldsymbol{\varepsilon}}, \qquad \mathbb{C}^0 = \frac{\partial^2 \varphi(\boldsymbol{\varepsilon})}{\partial \boldsymbol{\varepsilon}^2}, \tag{11.24}$$

respectively. The general form for the principle of total virtual power of the RCE reads

$$\delta\mathcal{P} = \underbrace{\int_{\mathcal{B}^1 \cup \mathcal{B}^2} \left\{ \mathfrak{s} : \delta\dot{\mathfrak{e}} \right\} \mathrm{d}\mathcal{V}}_{\text{internal power}} - \underbrace{\left(\int_{\mathcal{A}^\Gamma} \left\{ \mathfrak{t} \cdot \delta\dot{\mathfrak{u}}_\Gamma \right\} \mathrm{d}\mathcal{A} + \int_{\partial\mathcal{V}_{\mathrm{RCE}}} \left\{ \mathfrak{T} \cdot \delta\dot{\mathfrak{u}} \right\} \mathrm{d}\mathcal{A} + \int_{\mathcal{V}_{\mathrm{RCE}}} \left\{ (\mathfrak{f}^{\mathrm{p}} - \mathfrak{f}^{\mathrm{a}}) \cdot \delta\dot{\mathfrak{u}} \right\} \mathrm{d}\mathcal{V} \right)}_{\text{external power}} = 0. \tag{11.25}$$

It is noteworthy that the internal power is defined by the stress power in the block subdomains $\mathcal{B}^1 \cup \mathcal{B}^2$. The external power consists of the traction power $\mathfrak{T} \cdot \delta\dot{\mathfrak{u}}$ at the external surface of the RCE domain $\partial\mathcal{V}_{\mathrm{RCE}}$. Besides, it may include some other constitutive characteristics, e.g. crack surface friction or cohesive traction. Hence, a virtual power term $\mathfrak{t} \cdot \delta\dot{\mathfrak{u}}_\Gamma$ within the crack surfaces $\mathcal{A}^\Gamma$ is necessarily included to depict the aforementioned considerations. Furthermore, the passive and active volume force power $(\mathfrak{f}^{\mathrm{p}} - \mathfrak{f}^{\mathrm{a}}) \cdot \delta\dot{\mathfrak{u}}$ within the RCE volume $\partial\mathcal{V}_{\mathrm{RCE}}$ is presented as well. For simplicities, the work at hand does not take the RCE surface traction power and the volume force power quantities into account, which simplifies Eq. (11.25) to

$$\delta\mathcal{P} = \int_{\mathcal{B}^1 \cup \mathcal{B}^2} \left\{ \mathfrak{s} : \delta\dot{\mathfrak{e}} \right\} \mathrm{d}\mathcal{V} - \int_{\mathcal{A}^\Gamma} \left\{ \mathfrak{t} \cdot \delta\dot{\mathfrak{u}}_\Gamma \right\} \mathrm{d}\mathcal{A} = 0. \tag{11.26}$$

Another notable point is that the constitutive behavior of the RCE blocks and the intact bulk material is not restricted to simple linear elasticity. In contrast, it can also be associated with nonlinear elasticity as well as inelasticity, even at finite strains.

The virtual power principle of the RCE always exists for an arbitrary rate of virtual crack deformation, i.e. $\delta\dot{\Gamma}^{\mathrm{I}}$ with $\mathrm{I} = 1,2,3$. As a result, the relation

$$\delta_\Gamma\mathcal{P} = \int_{\mathcal{B}^1 \cup \mathcal{B}^2} \left\{ -\mathfrak{s} : \sum_{\mathrm{I}=1}^{3} \delta\dot{\Gamma}^{\mathrm{I}} \mathfrak{P}^{\mathrm{I}} \right\} \mathrm{d}\mathcal{V} - \int_{\mathcal{A}^\Gamma} \left\{ \mathfrak{t} \cdot \sum_{\mathrm{I}=1}^{3} \delta\dot{\Gamma}^{\mathrm{I}} \mathfrak{l}_{\mathrm{c}}\, \mathfrak{n}^{\mathrm{I}} \right\} \mathrm{d}\mathcal{A} = 0 \tag{11.27}$$

exists, and the crack deformation Γ^{I} with $\mathrm{I} = 1,2,3$ can be consistently solved by a straightforward minimization method. Nevertheless, even a correct mathematical solution of Γ^{I} may possibly conflict with the physically correct crack deformation for a closing crack, i.e. a negative Γ^1 indicates crack surfaces penetrated instead of a stiff contact. In this regard, an additional constraint needs to be imposed to prevent penetrated crack surfaces, and to obtain a realistic crack deformation. The crack state is determined by a predictor-corrector procedure, which means prediction of an opening crack deformation and correction for a closing crack deformation.

11.2.3.1 Crack Opening

The initial guess is based on an opening crack deformation, the minimization problem leads to

$$\Gamma^{\mathrm{I}} = \arg\left\{ \min_{\Gamma^{1,2,3}\in\mathcal{R}} \mathcal{P}\left(\boldsymbol{\varepsilon}, \Gamma^1, \Gamma^2, \Gamma^3\right) \right\}. \tag{11.28}$$

Thereafter, the unique solution of Γ^{I} fulfills the equilibrium

$$\int_{\mathcal{B}^1\cup\mathcal{B}^2} \left\{ \mathfrak{s} : \mathfrak{P}^{\mathrm{I}} \right\} \mathrm{d}\mathcal{V} + \int_{\mathcal{A}^\Gamma} \left\{ \mathfrak{l}_{\mathrm{c}}\, \mathfrak{t}\cdot\mathfrak{n}^{\mathrm{I}} \right\} \mathrm{d}\mathcal{A} = 0, \qquad \text{where} \qquad \mathrm{I} = 1,2,3. \tag{11.29}$$

For a general nonlinear constitutive law with respect to the RCE blocks and bulk materials or a nonlinear definition of $\mathfrak{t}$ with respect to $\mathfrak{u}_\Gamma$, this equilibrium is characterized as nonlinear as well. Therefore, analytical solutions of the unknown Γ^{I} are not straightforward, and even sometimes not possible to obtain. As a result, an internal NEWTON-RAPHSON algorithm is postulated to solve the equilibrium in Eq. (11.29). The local residual $\mathcal{R}_{\Gamma^{\mathrm{I}}}$ is, thus, defined as

$$\begin{aligned} \mathcal{R}_{\Gamma^{\mathrm{I}}} &= \int_{\mathcal{B}^1\cup\mathcal{B}^2} \left\{ \mathfrak{s} : \mathfrak{P}^{\mathrm{I}} \right\} \mathrm{d}\mathcal{V} + \int_{\mathcal{A}^\Gamma} \left\{ \mathfrak{l}_{\mathrm{c}}\, \mathfrak{t}\cdot\mathfrak{n}^{\mathrm{I}} \right\} \mathrm{d}\mathcal{A} \\ &= \left(\mathcal{V}^1 + \mathcal{V}^2 \right) \mathfrak{s} : \mathfrak{P}^{\mathrm{I}} + \mathcal{A}^\Gamma\, \mathfrak{l}_{\mathrm{c}}\, \mathfrak{t}\cdot\mathfrak{n}^{\mathrm{I}} \\ &= \mathfrak{l}_{\mathrm{c}}^3 \left(\mathfrak{s} : \mathfrak{P}^{\mathrm{I}} + \mathfrak{t}\cdot\mathfrak{n}^{\mathrm{I}} \right) \end{aligned} \tag{11.30}$$

and the internal consistent tangent is derived as

$$\begin{aligned} \mathcal{K}_{\Gamma^{\mathrm{I}}\Gamma^{\mathrm{J}}} = -\frac{\partial \mathcal{R}_{\Gamma^{\mathrm{I}}}}{\partial \Gamma^{\mathrm{J}}} &= -\mathfrak{l}_{\mathrm{c}}^3 \left(\frac{\partial \mathfrak{s}}{\partial \Gamma^{\mathrm{J}}} : \mathfrak{P}^{\mathrm{I}} + \frac{\partial \mathfrak{t}}{\partial \Gamma^{\mathrm{J}}} \cdot \mathfrak{n}^{\mathrm{I}} \right) \\ &= -\mathfrak{l}_{\mathrm{c}}^3 \left(\mathfrak{P}^{\mathrm{I}} : \frac{\partial \mathfrak{s}}{\partial \mathfrak{e}} : \frac{\partial \mathfrak{e}}{\partial \Gamma^{\mathrm{J}}} + \mathfrak{n}^{\mathrm{I}} \cdot \frac{\partial \mathfrak{t}}{\partial \mathfrak{u}_\Gamma} \cdot \frac{\partial \mathfrak{u}_\Gamma}{\partial \Gamma^{\mathrm{J}}} \right) \\ &= \mathfrak{l}_{\mathrm{c}}^3 \left(\mathfrak{P}^{\mathrm{I}} : \mathfrak{C} : \mathfrak{P}^{\mathrm{J}} - \mathfrak{l}_{\mathrm{c}}\, \mathfrak{n}^{\mathrm{I}} \cdot \mathfrak{k} \cdot \mathfrak{n}^{\mathrm{J}} \right), \end{aligned} \tag{11.31}$$

where $\mathfrak{k} = \partial \mathfrak{t} / \partial \mathfrak{u}_\Gamma$ is defined. The internal iteration algorithm is illustratively shown in **Table 11.1**. It is noteworthy that the trial state of the crack deformation $\Gamma^{\mathrm{I,tr}}_{\mathrm{k}=0}$ in **Table 11.1** can be numerically implemented as a history variable, which consists of values of the previous loading step. This algorithmic treatment yields a relatively fast local convergence to a certain extent.

Table 11.1: Internal NEWTON-RAPHSON iteration to obtain the RCE crack deformation quantities Γ^{I}.

Initiation	$k = 0, \quad \Gamma^{\mathrm{I}}_k = \Gamma^{\mathrm{I,tr}}_k$
Do Loop	
Residual	$\mathcal{R}_{\Gamma^{\mathrm{I}}} = l_c^3 \left(\mathfrak{s} : \mathfrak{P}^{\mathrm{I}} + \mathfrak{t} \cdot \mathfrak{n}^{\mathrm{I}} \right)$
Linearization	$\mathrm{Lin}\,\mathcal{R}_{\Gamma^{\mathrm{I}}} = \mathcal{R}_{\Gamma^{\mathrm{I}}}\Big\|_{\Gamma^{\mathrm{I}}_k} + \dfrac{\partial \mathcal{R}_{\Gamma^{\mathrm{I}}}}{\partial \Gamma^{\mathrm{J}}}\Big\|_{\Gamma^{\mathrm{I}}_k} \Delta\Gamma^{\mathrm{J}}_k$
Tangent	$\mathcal{K}_{\Gamma^{\mathrm{I}}\Gamma^{\mathrm{J}}} = -\dfrac{\partial \mathcal{R}_{\Gamma^{\mathrm{I}}}}{\partial \Gamma^{\mathrm{J}}}\Big\|_{\Gamma^{\mathrm{I}}_k}$
Solving	$\Delta\Gamma^{\mathrm{J}}_k = (\mathcal{K})^{-1}_{\Gamma^{\mathrm{J}}\Gamma^{\mathrm{I}}}\, \mathcal{R}_{\Gamma^{\mathrm{I}}}$
Update	$\Gamma^{\mathrm{J}}_{k+1} = \Gamma^{\mathrm{J}}_k + \Delta\Gamma^{\mathrm{J}}_k, \; k = k+1$
While	$\mathrm{Tol} \leqslant \Vert \mathcal{R}_{\Gamma^{\mathrm{I}}} \Vert$

11.2.3.2 Crack Closing

After the initial guess of crack opening prediction, the realistic crack deformation can be identified, i.e. opening or closing. Once the condition $\Gamma^1 < 0$ is fulfilled, the correction of a closing crack deformation is triggered. Thereafter, a mathematical constraint is artificially imposed to the new equilibrium and the relation in Eq. (11.27) is substituted by

$$\begin{aligned} &\Gamma^{2,3} = \arg \left\{ \min_{\Gamma^{2,3} \in \mathcal{R}} \mathcal{P}\left(\boldsymbol{\varepsilon}, \Gamma^2, \Gamma^3\right) \Big|_{\Gamma^1 = 0} \right\} \quad \text{for} \quad \Gamma^1 < 0, \\ &\Gamma^1 = 0. \end{aligned} \tag{11.32}$$

From the numerical point of view, the implementation of such a constraint condition may potentially lead to oscillations between opening and closing cracks. That phenomenon is investigated when Γ^1 is within an interval around the contact point, where the interval size is in the order of the numerical precision for the calculation of Γ^1. To obtain a relatively stable contact condition, a numerical assumption by setting a contact tolerance Tol is employed in order to detect the change of a contact state. In this regard, the contact triggering condition is redefined as

$$\Gamma^1 \leqslant \mathrm{Tol}, \tag{11.33}$$

where the tolerance Tol can be a sufficiently small and positive number, e.g., $\mathrm{Tol} = 10^{-12}$. Introducing the constraint $\Gamma^1 = 0$, the block strain in Eq. (11.22) needs to be rewritten as

$$\mathfrak{e} = \boldsymbol{\varepsilon} - \Gamma^1 \mathfrak{P}^1 - \Gamma^2 \mathfrak{P}^2. \tag{11.34}$$

The RCE stress $\mathfrak{s}$ and tangent $\mathfrak{C}$ as well as the crack surface tractions $\mathfrak{t}$ and its tangent $\mathfrak{k} = \partial \mathfrak{t} / \partial \mathfrak{u}_\Gamma$ in Eq. (11.31) are necessarily rederived based on the constraint condition. Reperforming the NEWTON-RAPHSON iteration in **Table 11.1** using the updated quantities, the crack deformations Γ^{I} with $\mathrm{I} = 2,3$ for the closing state are eventually obtained. The solution procedure is given in **Fig. 11.2**.

11.3 Regularization of the Free Discontinuity Problem

11.3.1 Governing Equations

The free discontinuity problem for brittle fracture with conservative external forces reads

$$\mathcal{E}\left(\mathbf{u}, \mathcal{B}^\Gamma\right) = \int_{\mathcal{B}\setminus\mathcal{B}^\Gamma} \varphi\left(\nabla \mathbf{u}\right) \mathrm{d}V + \mathcal{G}_{\mathrm{c}}\, \mathcal{H}^2\left(\mathcal{B}^\Gamma\right) \quad \longrightarrow \quad \min_{\mathbf{u}, \mathcal{B}^\Gamma} \mathcal{E}\left(\mathbf{u}, \mathcal{B}^\Gamma\right), \tag{11.35}$$

where the strain energy density φ is defined on the domain of the bulk material $\mathcal{B}\setminus\mathcal{B}^\Gamma$. The fracture energy is given by the fracture toughness $\mathcal{G}_{\mathrm{c}}$ and the area of crack surfaces $\mathcal{H}^2\left(\mathcal{B}^\Gamma\right)$. Different regularization methodologies are proposed for this variational problem. The regularization in eigenfracture yields

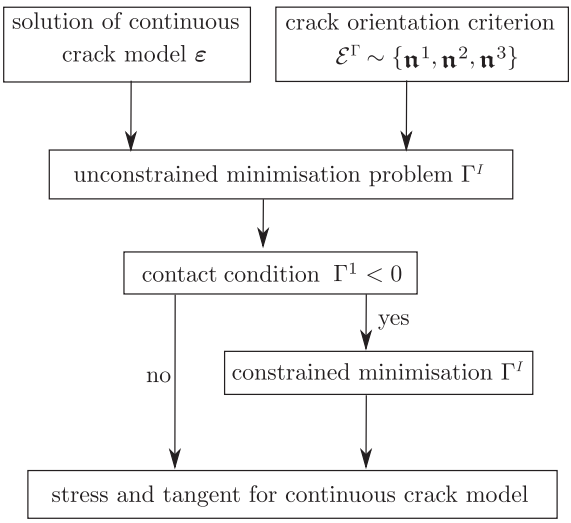

Fig. 11.2 Solution procedure for the RCE with homogeneous block deformations

$$\mathcal{E}(\boldsymbol{u},\boldsymbol{\varepsilon}^*) = \int_{\mathcal{B}} \varphi(\boldsymbol{\varepsilon}-\boldsymbol{\varepsilon}^*)\,\mathrm{d}V + \frac{\mathcal{G}_c}{2\epsilon}\,|\mathcal{B}^\epsilon| \quad \longrightarrow \quad \min_{\boldsymbol{u},\boldsymbol{\varepsilon}^*} \mathcal{E}(\boldsymbol{u},\boldsymbol{\varepsilon}^*) \tag{11.36}$$

with the approximated crack surfaces

$$\mathcal{B}^\epsilon := \left\{ \boldsymbol{X} \in \mathcal{B} \,\middle|\, \exists\, \boldsymbol{a} \in \mathrm{supp}(\boldsymbol{\varepsilon}^*)\,; \epsilon \geqslant |\boldsymbol{a}-\boldsymbol{X}| \right\}, \tag{11.37}$$

and the regularization in phase-field fracture reads

$$\mathcal{E}(\boldsymbol{u},\mathrm{d},\nabla\mathrm{d}) = \int_{\mathcal{B}} \varphi(\boldsymbol{\varepsilon})\,\mathrm{d}V + \mathcal{G}_c \int_{\mathcal{B}} \gamma_\mathrm{l}(\mathrm{d},\nabla\mathrm{d})\,\mathrm{d}V \;\longrightarrow\; \min_{\boldsymbol{u},\mathrm{d}} \mathcal{E}(\boldsymbol{u},\mathrm{d},\nabla\mathrm{d}). \tag{11.38}$$

Herein, new variables are added to the energy formulation, namely the phase-field variable d and the eigenstrain $\boldsymbol{\varepsilon}^*$. For regularized eigenfracture, the ϵ-neighborhood $\mathcal{B}^\epsilon$ of the support of the eigenstrain can be determined a posteriori to the mechanical equilibrium, and allows to introduce the eigenstrain $\boldsymbol{\varepsilon}^*$ as an internal variable. Nevertheless, the phase-field regularization of the crack area by means of $\gamma_\mathrm{l}(\mathrm{d},\nabla\mathrm{d})$ involves spacial gradients of the phase-field. Thus, it requires the phase-field variable d to be introduced as global state variable. A common crack surface density for the multi-dimensional problem is defined as

$$\gamma_\mathrm{l} = \frac{1}{2\mathrm{l}}\left(\mathrm{d}^2 + \mathrm{l}^2|\nabla_{\boldsymbol{X}}\mathrm{d}|^2\right), \tag{11.39}$$

where the internal length scale l is employed to govern the width of the transition zone between fractured ($\mathrm{d}=1$) and sound state ($\mathrm{d}=0$) of the material. For several intensive studies of the length scale l with respect to discretization, it is referred to Miehe et al. (2010b); Zhang et al. (2017); Mandal et al. (2019). The crack surface density function in Eq. (11.39) is also known as the AT2 model, which yields an exponentially shaped crack profile. Furthermore, another common alternative to approximate the crack surface density function is the classical AT1 model (Pham et al., 2011), which is not main scope of the discussion in this work.

The strain energy in the eigenfracture and the phase-field regularization can be related to the two material states φ^0 and φ^c, which are expressed by

$$\begin{aligned} &\varphi(\boldsymbol{\varepsilon}-\boldsymbol{\varepsilon}^*) = \begin{cases} \varphi^\mathrm{c}, & \text{for } \boldsymbol{X} \in \mathrm{supp}(\boldsymbol{\varepsilon}^*), \\ \varphi^0, & \text{else}, \end{cases} \\ &\text{and} \quad \varphi = \varphi^\mathrm{c}\left(\boldsymbol{\varepsilon},\Gamma^\mathrm{I}\right) + \mathrm{g}(\mathrm{d})\left(\varphi^0(\boldsymbol{\varepsilon}) - \varphi^\mathrm{c}\left(\boldsymbol{\varepsilon},\Gamma^\mathrm{I}\right)\right), \end{aligned} \tag{11.40}$$

respectively. Thus, the regularizations of the strain energy in eigenfracture and phase-field fracture are based on the behavior of intact material φ^0, i.e. in absence of a crack, and of fully broken material φ^c, i.e. in presence of a crack. While the intact material is described by classical constitutive models, the material behavior in the presence of a crack can be derived from an RCE.

Neglecting the derivation process based on a straightforward variational principle, the governing equations for the RCE problem read

$$\rho\,\ddot{\mathbf{u}} - \nabla_{\mathbf{X}} \cdot \boldsymbol{\sigma} - \mathbf{b} = \mathbf{0} \quad \text{in} \quad \mathcal{B} \qquad \text{and} \qquad \boldsymbol{\sigma} \cdot \mathbf{n} = \mathbf{t} \quad \text{at} \quad \partial\mathcal{B} \tag{11.41}$$

and

$$\int_{\mathcal{B}^1 \cup \mathcal{B}^2} \left\{ \mathfrak{s} : \mathfrak{P}^{\mathrm{I}} \right\} \mathrm{d}\mathcal{V} + \int_{\mathcal{A}^\Gamma} \left\{ \mathrm{l_c}\, \mathbf{t} \cdot \mathbf{n}^{\mathrm{I}} \right\} \mathrm{d}\mathcal{A} = 0 \quad \text{in} \quad \mathcal{V}_{\mathrm{RCE}} \quad \text{with} \quad \mathrm{I} = 1,2,3 \tag{11.42}$$

for the continuous deformation equilibrium and the RCE response, respectively. The notation $\nabla_{\mathbf{X}} \cdot (*)$ represents a divergence operator. The evolution equilibrium in Eq. (11.42) exactly coincides with the virtual power principle of Eq. (11.26) and the solution of crack deformation is according to the minimization problem Eq. (11.27). For eigenfracture modeling, the eigenstrain $\boldsymbol{\varepsilon}^*$ is regarded as an internal quantity, and the fracture evolution process is mainly based on a post-processing technique according to an ϵ-neighborhood algorithm. Nevertheless, in particular for phase-field fracture modeling, a degree of freedom is necessary to model fracture evolution, and the governing equation eventually reads

$$\partial_{\mathrm{d}}\, g(\mathrm{d}) \left(\varphi^0 - \varphi^{\mathrm{c}} \right) + \frac{\mathcal{G}_{\mathrm{c}}}{\mathrm{l}} \left(\mathrm{d} - \mathrm{l}^2 \nabla_{\mathbf{X}} \cdot \mathrm{d} \right) = 0 \ \text{ in } \ \mathcal{B} \quad \text{and} \quad \nabla_{\mathbf{X}} \mathrm{d} \cdot \mathbf{n} = 0 \ \text{ at } \ \partial\mathcal{B}. \tag{11.43}$$

The phase-field driving force term $\left(\varphi^0 - \varphi^{\mathrm{c}} \right)$ is based on two types of definitions, i.e. a damage-like approximation (Miehe et al., 2010a) or a fracture-like approximation (Kuhn and Müller, 2010).

11.3.2 Stress and Consistent Tangent

According to a straightforward derivation, the stress response and the consistent material tangent can be derived from the total effective HELMHOLTZ energy density function for both eigenfracture and phase-field fracture. In the intact material, the stress $\boldsymbol{\sigma}^0$ and the consistent tangent $\mathbb{C}^0$ can be straightforwardly derived based on the constitutive law, see Eqs. $(11.24)_1$ and $(11.24)_3$, respectively. However, with respect to the RCE description, the stress and material tangent tensors are obtained indirectly. Basically, the stress for the fully cracked state is characterized to be the RCE stress, i.e., $\boldsymbol{\sigma}^{\mathrm{c}} = \mathfrak{s}$. The consistent tangent $\mathbb{C}^{\mathrm{c}}$ yields

$$\begin{aligned}\mathbb{C}^{\mathrm{c}} = \frac{\mathrm{d}\,\boldsymbol{\sigma}^{\mathrm{c}}}{\mathrm{d}\,\boldsymbol{\varepsilon}} &= \frac{\mathrm{d}\,\mathfrak{s}}{\mathrm{d}\,\boldsymbol{\varepsilon}} \\ &= \frac{\partial\,\mathfrak{s}}{\partial\,\boldsymbol{\varepsilon}} + \sum_{\mathrm{J}=1}^{3} \frac{\partial\,\mathfrak{s}}{\partial\,\Gamma^{\mathrm{J}}} \otimes \frac{\partial\,\Gamma^{\mathrm{J}}}{\partial\,\boldsymbol{\varepsilon}} \\ &= \frac{\partial\,\mathfrak{s}}{\partial\,\boldsymbol{\varepsilon}} + \sum_{\mathrm{J}=1}^{3} \left(\frac{\partial\,\mathfrak{s}}{\partial\,\mathfrak{e}} : \frac{\partial\,\mathfrak{e}}{\partial\,\Gamma^{\mathrm{J}}} \right) \otimes \frac{\partial\,\Gamma^{\mathrm{J}}}{\partial\,\boldsymbol{\varepsilon}} \\ &= \mathfrak{C} + \sum_{\mathrm{J}=1}^{3} \left(-\mathfrak{C} : \mathfrak{P}^{\mathrm{J}} \right) \otimes \frac{\partial\,\Gamma^{\mathrm{J}}}{\partial\,\boldsymbol{\varepsilon}},\end{aligned} \tag{11.44}$$

where the partial derivative $\partial\,\Gamma^{\mathrm{J}}/\partial\,\boldsymbol{\varepsilon}$ cannot be derived in a straightforward manner. Therefore, by making use of the unconditional equilibrium of the minimization, one obtains the term $\partial\,\Gamma^{\mathrm{J}}/\partial\,\boldsymbol{\varepsilon}$ indirectly, reading

$$\begin{aligned}\mathcal{R}_{\Gamma^{\mathrm{I}}} = 0 \qquad &\Rightarrow \qquad \frac{\mathrm{d}\,\mathcal{R}_{\Gamma^{\mathrm{I}}}}{\mathrm{d}\,\boldsymbol{\varepsilon}} = \mathbf{0} \\ &\Rightarrow \qquad \frac{\partial\,\mathcal{R}_{\Gamma^{\mathrm{I}}}}{\partial\,\boldsymbol{\varepsilon}} + \sum_{\mathrm{J}=1}^{3} \left(\frac{\partial\,\mathcal{R}_{\Gamma^{\mathrm{I}}}}{\partial\,\Gamma^{\mathrm{J}}} \frac{\partial\,\Gamma^{\mathrm{J}}}{\partial\,\boldsymbol{\varepsilon}} \right) = \mathbf{0} \\ &\Rightarrow \qquad \frac{\partial\,\mathcal{R}_{\Gamma^{\mathrm{I}}}}{\partial\,\mathfrak{s}} : \frac{\partial\,\mathfrak{s}}{\partial\,\mathfrak{e}} : \frac{\partial\,\mathfrak{e}}{\partial\,\boldsymbol{\varepsilon}} = \sum_{\mathrm{J}=1}^{3} \left(-\frac{\partial\,\mathcal{R}_{\Gamma^{\mathrm{I}}}}{\partial\,\Gamma^{\mathrm{J}}} \frac{\partial\,\Gamma^{\mathrm{J}}}{\partial\,\boldsymbol{\varepsilon}} \right) \\ &\Rightarrow \qquad -\mathfrak{P}^{\mathrm{I}} : \mathfrak{C} : \mathbb{I} = \sum_{\mathrm{J}=1}^{3} \left(\mathcal{K}_{\Gamma^{\mathrm{I}}\Gamma^{\mathrm{J}}} \frac{\partial\,\Gamma^{\mathrm{J}}}{\partial\,\boldsymbol{\varepsilon}} \right) \\ &\Rightarrow \qquad \frac{\partial\,\Gamma^{\mathrm{J}}}{\partial\,\boldsymbol{\varepsilon}} = -\sum_{\mathrm{I}=1}^{3} \left(\left(\mathcal{K}^{-1}\right)_{\Gamma^{\mathrm{J}}\Gamma^{\mathrm{I}}} \mathfrak{C} : \mathfrak{P}^{\mathrm{I}} \right).\end{aligned} \tag{11.45}$$

As a result, substituting Eq. (11.45) into Eq. (11.44), the consistent tangent tensor for the fully cracked material yields

$$\begin{aligned}\mathbb{C}^{\mathrm{c}} &= \mathfrak{C} + \sum_{\mathrm{J}=1}^{3} \sum_{\mathrm{I}=1}^{3} \left(-\mathfrak{C} : \mathfrak{P}^{\mathrm{J}} \right) \otimes \left(-\left(\mathcal{K}^{-1}\right)_{\Gamma^{\mathrm{J}}\Gamma^{\mathrm{I}}} \mathfrak{C} : \mathfrak{P}^{\mathrm{I}} \right) \\ &= \mathfrak{C} + \sum_{\mathrm{J}=1}^{3} \sum_{\mathrm{I}=1}^{3} \left(\mathcal{K}^{-1}\right)_{\Gamma^{\mathrm{J}}\Gamma^{\mathrm{I}}} \left(\mathfrak{C} : \mathfrak{P}^{\mathrm{J}} \right) \otimes \left(\mathfrak{C} : \mathfrak{P}^{\mathrm{I}} \right),\end{aligned} \tag{11.46}$$

Thus, based on Eq. $(11.40)_1$, the deformation response can be straightforwardly formulated within an eigenfracture framework, since

$$\boldsymbol{\sigma} = \begin{cases} \boldsymbol{\sigma}^{\mathrm{c}}, & \text{for } \mathbf{X} \in \operatorname{supp}(\boldsymbol{\varepsilon}^{*}), \\ \boldsymbol{\sigma}^{0}, & \text{else}, \end{cases} \qquad \text{and} \qquad \mathbb{C} = \begin{cases} \mathbb{C}^{\mathrm{c}}, & \text{for } \mathbf{X} \in \operatorname{supp}(\boldsymbol{\varepsilon}^{*}), \\ \mathbb{C}^{0}, & \text{else}. \end{cases} \tag{11.47}$$

Nonetheless, for a variational phase-field fracture modeling, a further manipulation needs to be accounted for according to the similar relationship in Eq. $(11.40)_2$, namely

$$\boldsymbol{\sigma} = \boldsymbol{\sigma}^{\mathrm{c}} + \mathrm{g}(\mathrm{d})\left(\boldsymbol{\sigma}^{0} - \boldsymbol{\sigma}^{\mathrm{c}}\right) \qquad \text{and} \qquad \mathbb{C} = \mathbb{C}^{\mathrm{c}} + \mathrm{g}(\mathrm{d})\left(\mathbb{C}^{0} - \mathbb{C}^{\mathrm{c}}\right). \tag{11.48}$$

11.4 Numerical Applications

This section introduces a comprehensive application of eigenfracture and phase-field fracture modeling within an RCE framework with respect to different model problems. Each constitutive approach is consistently derived and implemented into an in-house simulation platform.

11.4.1 Self-consistent Test

Phenomenologically, without considering cohesive traction and friction at crack surfaces, an open-crack leads to a stress-free boundary. A closed and friction-free crack at a compressive state is supposed to fully transfer the normal compressive stress, which is characterized as an equivalent contact mechanism. Furthermore, a pure shear deformation along the friction-free crack surface should not transfer any force neither. The aforementioned characteristics have been studied in Steinke and Kaliske (2019); Strobl and Seelig (2016); Storm et al. (2020) to evaluate the correct phase-field crack kinematics for realistic applications. The first numerical example, herein, attempts to examine the crack kinematics to demonstrate the advantages of the presented eigenfracture and phase-field modeling in an RCE description compared to the classical spectral split and the V-D split approaches with respect to tension, compression and shearing deformation.

The two-dimensional boundary value problem is depicted in **Fig. 11.3**, which consists of a contact model, an eigenfracture model, and a phase-field model with the same dimensions. The contact model consists of two blocks and a contact pair. The eigenfracture model depicts the crack using a row of fully eroded elements, and the phase-field model describes the straight crack by prescribing the phase-field value $\mathrm{d} = 1$ at the nodes attached to the middle row of elements. All models are discretized by 2500 four-node elements uniformly with the element size $\mathrm{h}_e = 2\,\mathrm{mm}$. The upper and lower edges are fully bounded and a displacement load is subjected to the upper edge with a loading function given in **Fig. 11.4** for tension, compression and shear deformation in a linear elastic body as well as compressive relaxation for linear viscoelasticity.

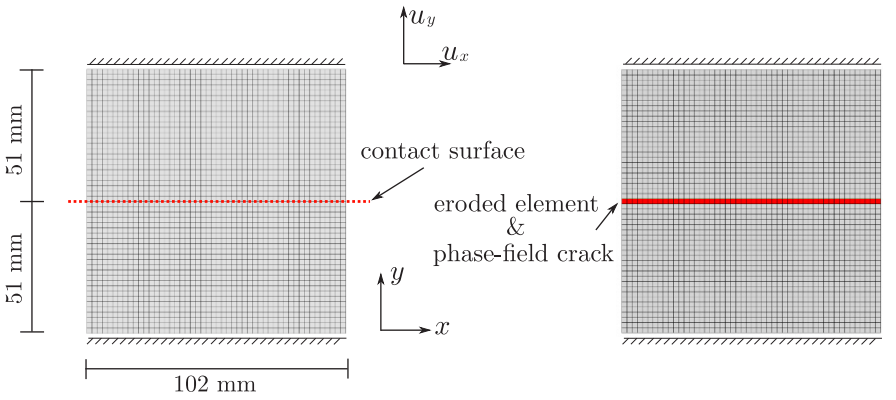

Fig. 11.3: Geometric setup for contact surface and phase-field crack.

11.4.1.1 Linear Elasticity

The simulations are based on the spectral split, V-D split as well as the RCE description of both eigenfracture and RCE phase-field modeling. The material parameters are given as $\lambda = 19.6\,\text{MPa}$, $\mu = 2.06\,\text{MPa}$ for linear elasticity. Based on the loading in **Fig. 11.4** (a), the RCE eigenfracture results are shown in **Fig. 11.5** (with $\epsilon = 14\,\text{mm}$), and the RCE phase-field solutions are shown in **Fig. 11.6** (with $\mathrm{l} = 4\,\text{mm}$). Apparently, the three simulations, the spectral split, the V-D split and the RCE approach, have obtained realistic crack opening deformations compared to the reference discrete crack simulation, i.e. non residual material deformations exist in the upper and lower block at the maximum separation $\mathrm{t} = 1$ s. In the sequel, the material is compressed and both the spectral and the V-D split simulations are not capable to

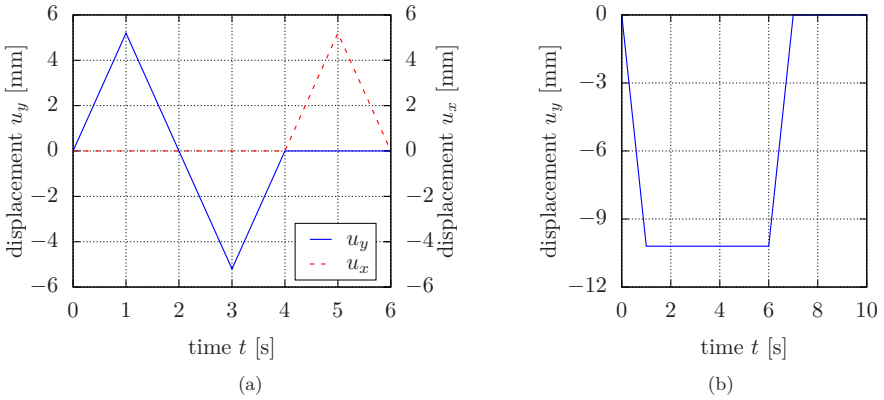

Fig. 11.4: Displacement loading function at (a) tension, compression and shear deformation for linear elasticity and only at (b) compression and relaxation for linear viscoelasticity.

capture the realistic crack closing deformations at $t = 3$ s. A slight unphysical lateral expansion by the spectral split is obtained. Unfortunately, this lateral expansion is significantly increased by the V-D split result. Nevertheless, this unphysical behavior does not appear at all for the proposed RCE modeling. Furthermore, the spectral split result fails to capture a realistic shear deformation at the crack, see **Figs. 11.5** (b) and **11.6** (a).

11.4.1.2 Linear Viscoelasticity

It is noteworthy that the constitutive laws in Steinke and Kaliske (2019); Strobl and Seelig (2016); Storm et al. (2020) are restricted to linear elasticity. Nevertheless, the RCE phase-field approach provides a general framework, which may be applied to any constitutive material model. For the total derivation, it is particularly referred to Yin et al. (2021). Furthermore, the RCE eigenfracture does not restrict the constitutive law as well. This work does not present the linear viscoelasticity model for an RCE eigenfracture description, but it is one of the next priorities for future publications. Due to linearity of the material, the RCE phase-field formulation aforementioned eventually returns to a relatively simple problem. The material tangent tensors for both bulk material and RCE blocks, i.e. $\mathbb{C}^0$ and $\mathfrak{C}$ are always constant. Meanwhile, $\mathfrak{t}$ and $\mathfrak{k}$ vanish due to traction-free and friction-free considerations. As a result, the crack deformations $\Gamma^{1,2,3}$ (opening) or $\Gamma^{2,3}$ (closing) can be resolved by a closed form solution, which largely simplify the model problems.

It is necessary to point out that the standard spectral split (Miehe et al., 2010a) is not included for linear viscoelasticity due to some difficulties. The coupled constitutive equations of the spectral split model in Miehe et al. (2010a) are straightforwardly and consistently derived out of a predefined strain energy density functional involving the spectral decomposition of the strain tensor. However, the present linear viscoelastic model is governed by internal stress-type quantities, which cannot be obtained by a straightforward variational algorithm of strain based energy density function. Furthermore, the elastic energy for the non-equilibrium branches is obtained based on the non-equilibrium stress and the conjugate elastic tensor due to the constitutive linear characteristics. Therefore, the spectral split of the internal stress governed viscoelastic model has shown significant complexities. As a result, several existing phase-field models regarding fracture of viscoelastic material, see e.g. Shen et al. (2019); Schänzel (2015); Loew et al. (2019); Yin and Kaliske (2020c), are developed depending on the framework of the V-D split. Instead of the spectral split, a classical contact model is additionally considered for a representative reference for the crack kinematics demonstration in viscoelastic materials.

Another loading function in **Fig. 11.4** (b) describes pure compression and subsequent relaxation for the viscoelastic solid. The spectral split simulation is considered. Instead, classical contact modeling is performed. In a detailed description, the viscoelastic response of the material is supposed to relax from $t = 1$ s to $t = 6$ s at compressive state and from $t = 7$ s to $t = 10$ s at a non-external load state. Regarding viscoelasticity, only one PRONY term is considered and the parameters are given as

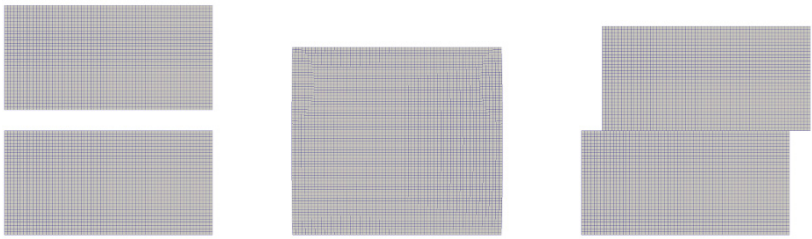

(a) deformation by discrete crack

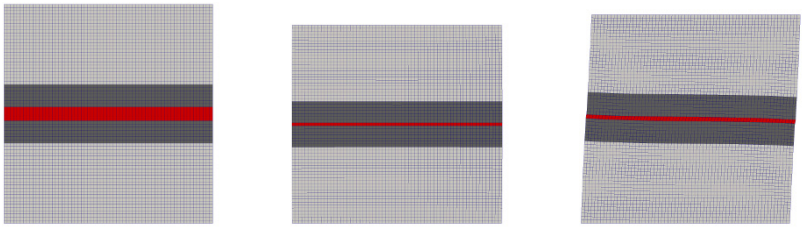

(b) deformation by spectral split

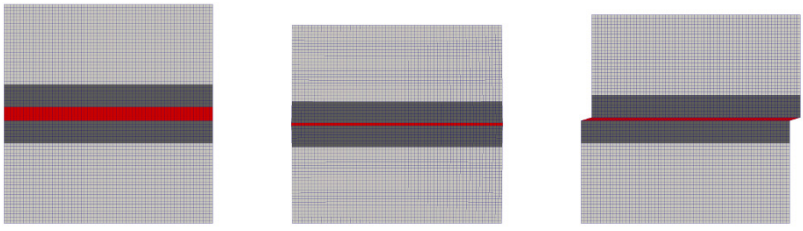

(c) deformation by V-D split

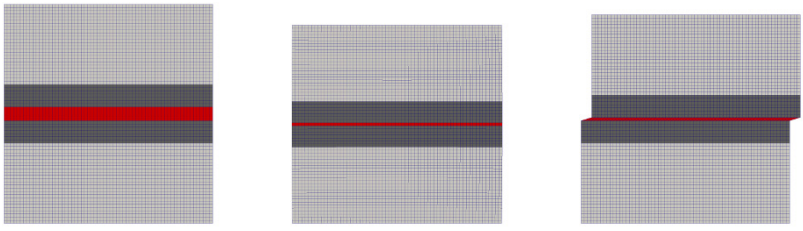

(d) deformation by RCE

Fig. 11.5: Crack deformation at $\mathtt{t} = 1\,\mathrm{s}$, $\mathtt{t} = 3\,\mathrm{s}$ and $\mathtt{t} = 5\,\mathrm{s}$ regarding the loading function in **Fig. 11.4** (a) for spectral split, V-D split and RCE approach using the eigenfracture approach.

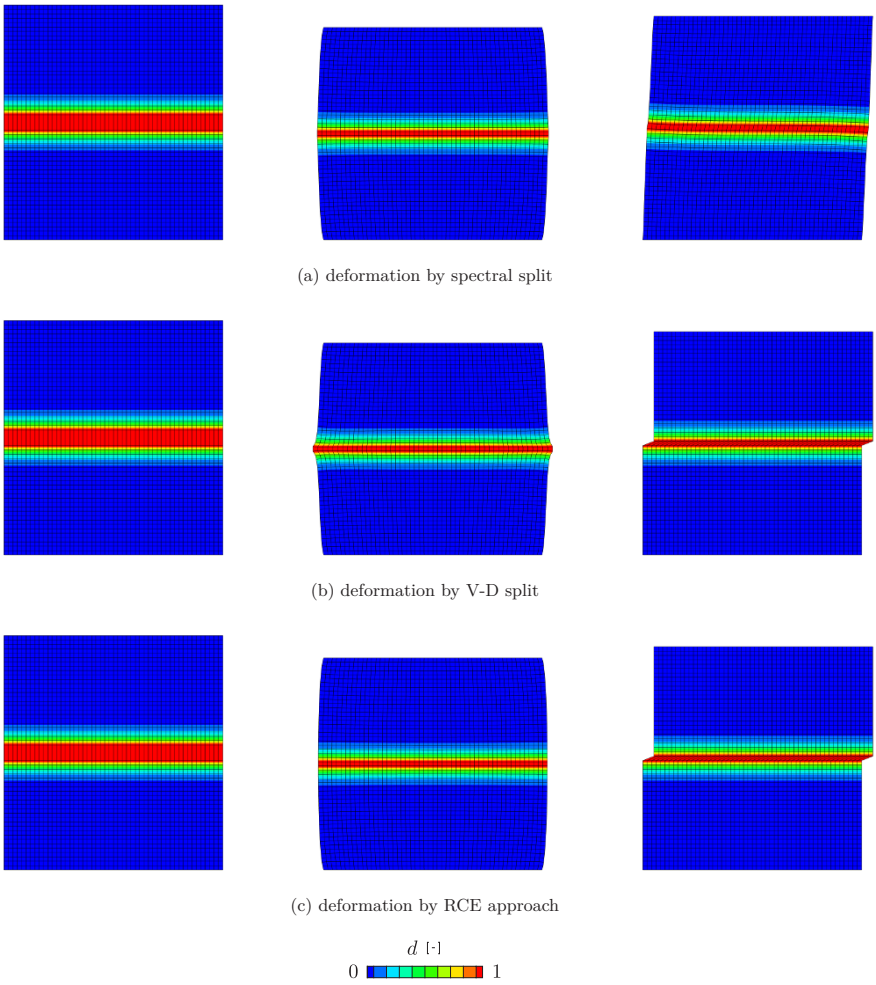

Fig. 11.6: Crack deformation at $t = 1\,s$, $t = 3\,s$ and $t = 5\,s$ regarding the loading function in **Fig. 11.4** (a) for spectral split, V-D split and RCE approach using phase-field modeling.

$\tau = 0.98\,s$ and $\chi = 0.6$. As aforementioned, the V-D split model is not capable of capturing an appropriate compressive deformation in a viscoelastic body neither due to an unrealistic lateral stretch. Nevertheless, the RCE simulation properly addresses this issue and shows similar behavior compared to the contact model. Meanwhile, the contour distributions of the vertical stress σ_y for three approaches are compared at $t = 1\,s$ and $t = 6\,s$ in **Fig. 11.7**, where the RCE modeling successfully predicts the results that the contact model shows.

Furthermore, the effective strain energy φ^{mech}, the viscous dissipation $\mathcal{W}^{vis}$ as well as their summation $\hat{\varphi} = \varphi^{mech} + \mathcal{W}^{vis}$ for the three models are evaluated. The V-D split model uses the standard form of $\varphi^{mech} = \varphi^{-} + g(d)\,\varphi^{+}$, where for the de-

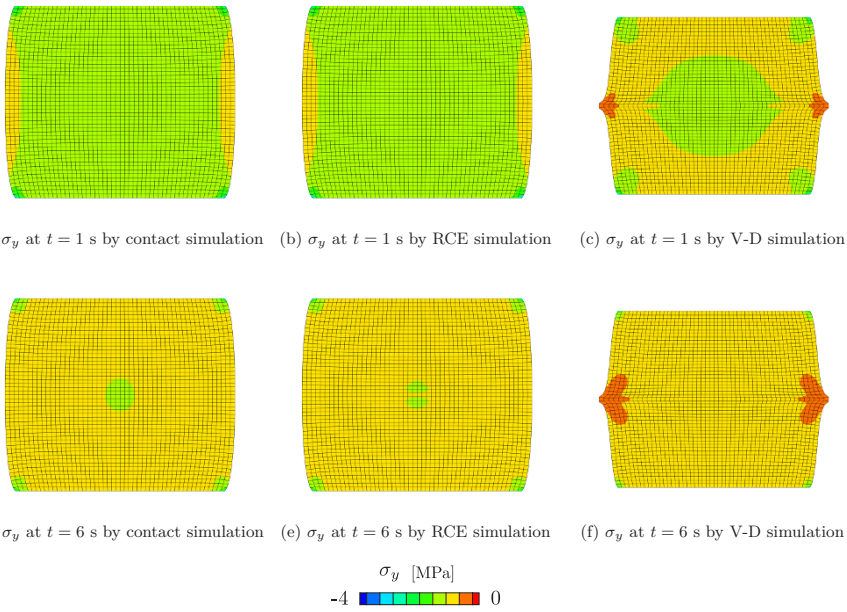

Fig. 11.7: Comparison of the distribution of the vertical stress σ_y for contact modeling, RCE simulation and V-D split simulation at $t = 1$ s (a)-(c) and $t = 6$ s (d)-(f), respectively.

tailed algorithmic setup, it is referred to Schänzel (2015); Yin and Kaliske (2020c). In the sequel, by a post-processing technique of volume integration of these two quantities, the total elastic strain energy and dissipation energy are obtained. Then, the quantity $\hat{\varphi} = \varphi^{\text{mech}} + \mathcal{W}^{\text{vis}}$ is also evaluated, since it straightforward indicates the external work induced into the closed system. Observing the energy components evolution in **Figs. 11.8** (a)-(c), φ^{mech} and $\mathcal{W}^{\text{vis}}$ increase initially along with the external load application. Subsequently, the constant load leads to a slight decrease of φ^{mech} and a gradual increase of $\mathcal{W}^{\text{vis}}$ up to the situation that the specimen is fully relaxed. The summation $\hat{\varphi}$ stays almost constant during the relaxation. It is explained that the external work does not change as long as the external load is kept constant. After the displacement returns to $u = 0$ mm and the material is fully relaxed, e.g. $t = 10$ s, φ^{mech} returns to 0 kJ and the total external work is fully dissipated due to viscous effects. Comparing these three approaches, the RCE formulation sufficiently agrees to the results of the contact modeling. However, the V-D split always underestimates the results, also see the reaction forces given in **Fig. 11.8** (d). Based on the aforementioned comments, the RCE approach is demonstrated to capture realistic crack kinematics for a closing crack within linear elastic and viscoelastic materials.

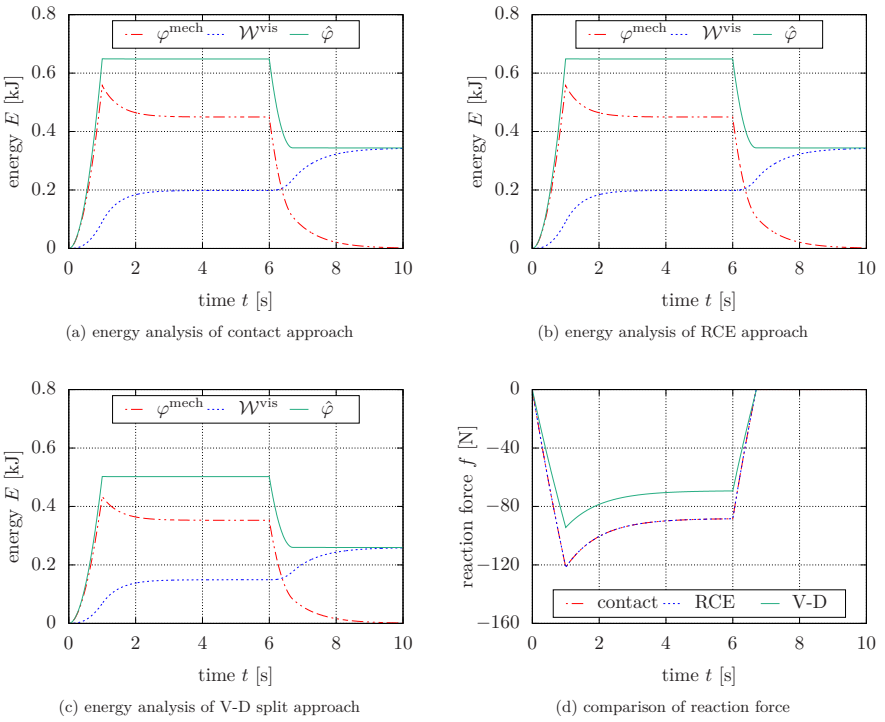

(a) energy analysis of contact approach

(b) energy analysis of RCE approach

(c) energy analysis of V-D split approach

(d) comparison of reaction force

Fig. 11.8: Investigation of energy components: elastic strain energy φ^{mech}, viscous dissipation energy $\mathcal{W}^{\mathrm{vis}}$ and their summation $\hat{\varphi} = \varphi^{\mathrm{mech}} + \mathcal{W}^{\mathrm{vis}}$ for (a) contact modeling, (b) RCE simulation and (c) V-D split simulation, (d) reaction force f for the three approaches.

11.4.2 A Single Edge Notch Plate (SENP) at Shear Load

Using the similar geometric setup as in Miehe et al. (2010a), an elastic plate of length 100 mm, which is cracked half by an initial notch, is studied in this example. The plate edges parallel to the crack are clamped, and one edge is displaced parallel to the crack, leading to shear failure. The elastic parameters are $\lambda = 121.15$ GPa, $\mu = 80.77$ GPa, the fracture toughness is $\mathcal{G}_c = 2.7$ N/mm^2 and the length scale for phase-field is $l = 0.2$ mm. The displacement application is linearly increasing with time. For the numerical discretization of the two-dimensional boundary value problem, a total of 27225 uniform quadrilateral elements for plane strain with linear shape functions are used. In particular, in the used eigenfracture implementation, a new mechanical equilibrium state is determined before the next most critical element may fracture. The simulations are performed using the eigenfracture approach based on well known spectral split (Miehe et al., 2010a) and the V-D split (Amor et al., 2009), as well as for the eigenfracture model based on the RCE framework. A noteworthy point for the RCE framework is that the crack orientation for each element is calculated at the GAUSS point applying a reduced integration scheme.

Regarding the simulation results of the *SENP* test, the crack evolution and the crack neighborhood ($\varepsilon = 30.1\,h_e$) are shown in **Figs. 11.9** (a) and (b). In particular, the crack paths of the models with the spectral split, V-D split, and based on the RCE framework are compared. In principle, considering frictionless features, the crack surfaces along the initial crack should slide on each other without force transfer through the crack. Using the spectral split, the result based on a discrete crack description significantly differs from the model with pre-eroded elements. Therefore, the spectral split approach cannot be equivalently used for a discrete and a numerical crack due to the unphysical force transfer through a sliding crack surface. The crack paths predicted by the V-D and the RCE model differ in the propagation angle. Furthermore, both models yield a crack broadening in the region of the initial crack tip. The broadening is possibly caused by the regularized formulation of the increment of the crack surface area. As a consequence, crack surface increments for crack propagation perpendicular to the crack ligament are systematically smaller than in the direction of the crack ligament. Moreover, crack surface increments behind the crack tip are systematically smaller than at the crack tip. Thus, the elastic energy required to propagate a crack is largest at the crack tip for cracks propagating towards the crack ligament.

In addition to the eigenfracture simulation, the phase-field approach is also employed to simulate the *SENP* cracking as a comparison, see **Figs. 11.9** (c) and (d). Based on the same reason, the spectral split crack is not capable of predicting the realistic crack evolution by prescribing a phase-field crack as the initial notch. Since the whole process of *SENP* shear does not introduce any compressive deformation, the V-D split and the RCE framework yield good agreement to each other regarding the crack path prediction. Nevertheless, as long as compressive deformation exists, the V-D split immediately fails to predict the correct crack path as aforementioned in Sect. 11.4.1.

Furthermore, the influence of the ε-neighborhood size is studied in **Fig. 11.10**. The simulation is performed for different values of ε on the same mesh. The load at which the crack begins to propagate in the simulation is evaluated for different value of ε. Apparently, **Fig. 11.10** shows that the maximum force converges asymptotically with increasing neighborhood size. Convergence of the results can be accepted for the presented study when the neighborhood size parameter ε is about 15 times the element size h_e. However, crack propagation is disturbed when the ε-neighborhood reaches the geometry boundary of the model, e.g., crack kinking.

11.4.3 Structural Fracture at Finite Strain

The presented example is performed to demonstrate the capability of the phase-field model applied to hyper-elastic material by studying a promising benchmark of polymer fracture. The experimental tests are conducted by Hocine et al. (2002) to estimate the critical fracture energy. In the sequel, this example is studied by several different numerical approaches, e.g. the material force method Özenç and Kaliske

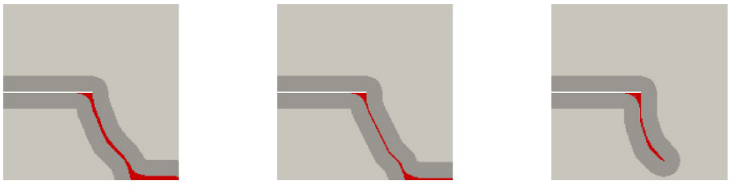

(a) eigenfracture with discrete crack for spectral split, V-D split and RCE, respectively

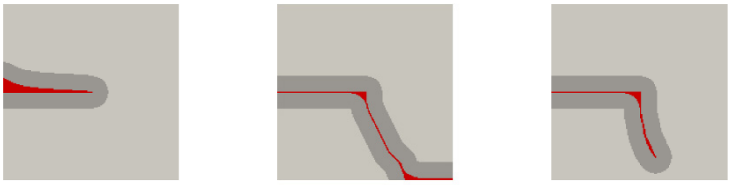

(b) eigenfracture with element erosion crack for spectral split, V-D split and RCE, respectively

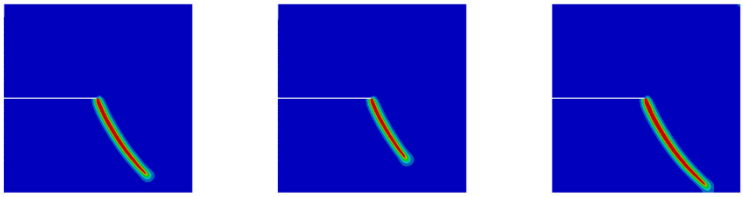

(c) phase-field with discrete crack for spectral split, V-D split and RCE, respectively

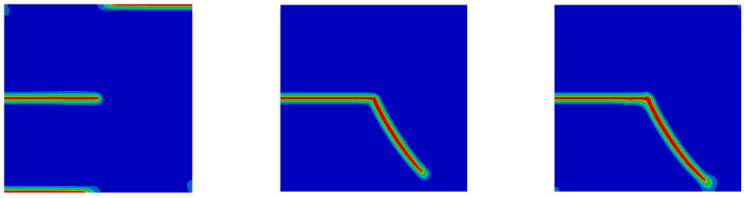

(d) phase-field with smeared phase-field crack for spectral split, V-D split and RCE, respectively

Fig. 11.9: Eigenfracture and phase-field simulation of crack evolution for both discrete crack and numerical crack (pre-eroded elements or phase-field crack) with respect to spectral split, V-D split and the RCE framework, respectively.

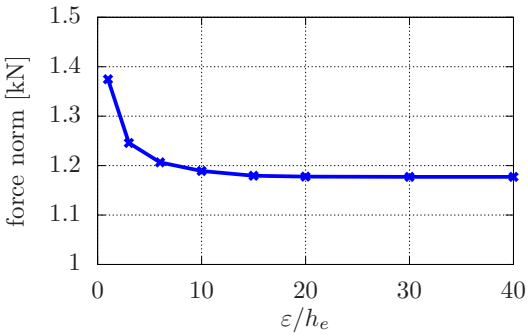

Fig. 11.10 Dependency of the maximum reaction force norm on the neighborhood size parameter ε.

(2014) and the phase-field model (Miehe and Schänzel, 2014), which show good agreement compared to the evaluations of Hocine et al. (2002).

Regarding the constitutive law, Özenç and Kaliske (2014) simulates polymer fracture using the ARRUDA-BOYCE model, whose HELMHOLTZ energy density function generally reads

$$\varphi^0 = \kappa\left(J - \ln J - 1\right) + \mu N\left(\lambda_r \mathcal{L}^{-1}\left(\lambda_r\right) + \ln\frac{\mathcal{L}^{-1}\left(\lambda_r\right)}{\sinh \mathcal{L}^{-1}\left(\lambda_r\right)}\right). \tag{11.49}$$

The segmentation N is a material parameter in addition to the bulk and shear moduli κ and μ. The stretch quantity λ_r is obtained by $\lambda_r = \sqrt{\mathrm{tr}\left(\bar{\mathbf{C}}\right)/3N}$, where $\bar{\mathbf{C}}$ is the isochoric part of the right CAUCHY-GREEN tensor, and the inverse LANGEVIN function is defined by $\mathcal{L}^{-1}$. By applying the phase-field approach, Miehe and Schänzel (2014) describes the polymer based on the compressible NEO-HOOKEAN formulation, whose energy density function is defined as

$$\varphi^0 = \frac{\mu}{\beta}\left(J^{-\beta} - 1\right) + \frac{\mu}{2}\left(\mathrm{tr}\left(\mathbf{C}\right) - 3\right), \tag{11.50}$$

where β and μ are two governing parameters. For the purpose of simplicity and generality, this work chooses a nearly incompressible NEO-HOOKEAN model, which depends on the energy density function

$$\varphi^0 = \kappa\left(J - \ln\left(J\right) - 1\right) + \frac{\mu}{2}\left(\mathrm{tr}\left(\bar{\mathbf{C}}\right) - 3\right). \tag{11.51}$$

As a result of a consistent and straightforward derivation, the intact KIRCHHOFF stress and the corresponding material tangent tensors yield

$$\boldsymbol{\tau}_0 = p\,\mathbf{1} + \underbrace{\mu\left(\bar{\mathbf{b}} - \frac{1}{3}\mathrm{tr}\left(\bar{\mathbf{C}}\right)\mathbf{1}\right)}_{\boldsymbol{\tau}_{iso}} \tag{11.52}$$

and

$$\mathbb{C}_0 = \Big(\mathrm{p}+\mathrm{s}\Big)\mathbf{1}\otimes\mathbf{1} - 2\mathrm{p}\,\mathbb{I} + \frac{2}{3}\Big(\mu\,\mathrm{tr}\big(\bar{\mathbf{C}}\big)\,\mathbb{P} - \boldsymbol{\tau}_{\mathrm{iso}}\otimes\mathbf{1} - \mathbf{1}\otimes\boldsymbol{\tau}_{\mathrm{iso}}\Big), \qquad (11.53)$$

respectively. The definition of the isochoric right and left CAUCHY-GREEN tensors are $\bar{\mathbf{C}} = \mathrm{J}^{\frac{2}{3}}\mathbf{C}$ and $\bar{\mathbf{b}} = \mathrm{J}^{\frac{2}{3}}\mathbf{b}$. The hydrostatic scalar p and its corresponding modulus are obtained based on the first and the second order partial derivative of the volumetric energy density with respect to J, i.e. $\mathrm{p} = \mathrm{J}\,\partial_{\mathrm{J}}\,\mathrm{U}(\mathrm{J})$ and $\mathrm{s} = \mathrm{J}^2\,\partial^2_{\mathrm{JJ}}\,\mathrm{U}(\mathrm{J})$.

According to the material description aforementioned, a two-dimensional boundary value problem is taken into account. The geometry and boundary condition setup are depicted in **Fig. 11.11**. The bottom edge is fully fixed and the top one is fixed by a vertical upward displacement, which leads to monotonic tensile failure. Three symmetrical notch widths $a_0 = [12, 20, 28]$ mm are evaluated. Due to the symmetric geometry, loading as well as boundary conditions, a simplification can be employed by only considering half of the original specimen with appropriate symmetry conditions. The finite element discretizations consist of approximately 1200 4-node quadratic elements, where the potential damage paths are meshed by the uniform element size $h_e = 1$ mm. The model parameters are given as $\kappa = 5.49$ MPa, $\mu = 0.57$ MPa, $\mathcal{G}_c^0 = 6.16\,\mathrm{J/mm^2}$ and the length-scale parameter for the phase-field evolution is $l = 2$ mm. The initial crack normal coincides with the loading direction.

The visualization of the phase-field crack evolution of the specimen with $a_0 = 20$ mm is shown in **Fig. 11.12**. With the help of a post-processing blanking technique, i.e. the phase-field value $d \geqslant 0.95$ is not visible, a vivid crack initiation and propagation before the complete separation can be effectively investigated. Furthermore, the load-displacement relations obtained by the present phase-field modeling are compared to the experimental results in **Fig. 11.13** for all the three specimen geometries. The fact of a smaller initial notch leading to larger overall strength is validated. Meanwhile, both the peak and the fracture displacements for the three cases can be approximately predicted. The force-displacement characteristics and the structural deformations are in good agreement with the experimental findings. Before structural rupture, a sudden drop of the reaction force along with unstable

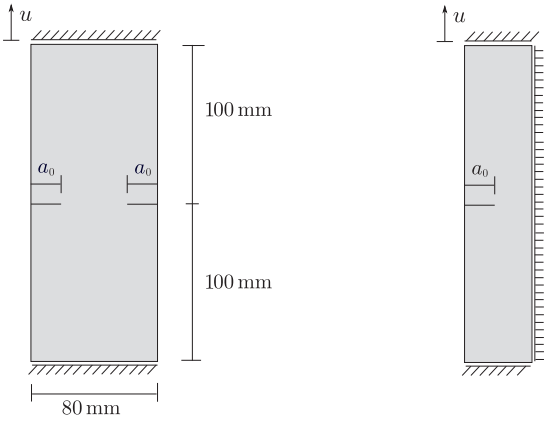

Fig. 11.11 (a) Geometrical setup of two-dimensional notched specimen and (b) its simplified half model due to symmetry.

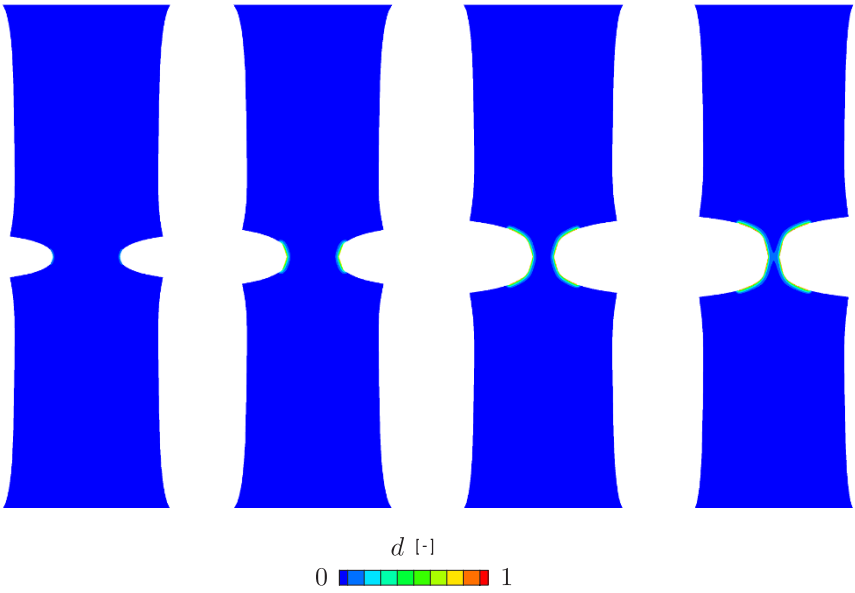

Fig. 11.12: Fracture evolution of the two-dimensional model by blanking the phase-field $\mathrm{d} \geqslant 0.95$.

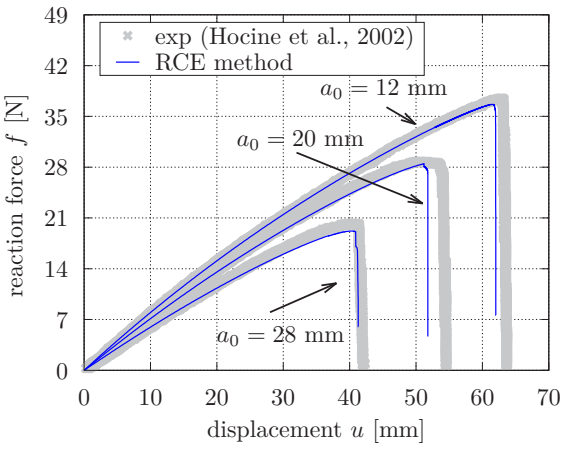

Fig. 11.13 Comparison of the load-displacement relations of styrene butadiene rubber obtained by experimental results (Hocine et al., 2002) to the present phase-field model.

crack growth is obtained. The numerical convergence of the model in this final part of the simulation is hard to achieve due to large distortions of the elements at the crack tip. Therefore, full rupture is not reached.

11.4.4 Cohesive Failure Modeling

The example at hand studies cohesive failure within an RCE phase-field framework. The mechanism is mainly governed by the classical traction-separation law, which is commonly taken into consideration by the interface element approach.

The cohesive traction at the crack surface denoted by $\mathbf{t}$ in Eq. (11.25) usually cannot be neglected. This term is defined to be oriented outwards at the crack surface and the direction opposite the crack surface deformation $\mathbf{u}_\Gamma$. Herein, a classical traction-separation law (van den Bosch et al., 2008) is considered, and the pseudo potential functional is defined as

$$\varphi_{TS} = \phi - \frac{(\|\mathbf{u}_\Gamma\| + \Delta)\,\phi}{\Delta} \exp\left(-\frac{\|\mathbf{u}_\Gamma\|}{\Delta}\right), \tag{11.54}$$

where ϕ is a model parameter to represent the work or energy of separation and Δ is another parameter for the characteristic opening length. The maximum tractions T_{max} can be indirectly calculated by means of $T_{max} = \phi/(\exp(1)\,\Delta)$. According to variational derivation, the surface traction is derived as

$$\mathbf{t} = -\frac{\partial \varphi_{TS}}{\partial \mathbf{u}_\Gamma} = -\frac{\phi}{\Delta^2} \exp\left(-\frac{\|\mathbf{u}_\Gamma\|}{\Delta}\right) \mathbf{u}_\Gamma, \qquad \text{where} \qquad \mathbf{u}_\Gamma = \sum_{I=1}^{3} l_c\, \Gamma^I\, \mathbf{n}^I \tag{11.55}$$

and the consistent tangent reads

$$\mathbb{t} = \frac{\partial^2 \varphi_{TS}}{\partial \mathbf{u}_\Gamma^2} = -\frac{\partial \mathbf{t}}{\partial \mathbf{u}_\Gamma} = \frac{\phi}{\Delta^2} \exp\left(-\frac{\|\mathbf{u}_\Gamma\|}{\Delta}\right) \left(\mathbf{1} - \frac{\mathbf{u}_\Gamma \otimes \mathbf{u}_\Gamma}{\Delta\,\|\mathbf{u}_\Gamma\|}\right). \tag{11.56}$$

The aforementioned traction and tangent quantities characterize the path independent traction-separation formulation, which describe crack healing phenomena of the unloading and reloading processes. In order to achieve a general damage-like formulation, an algorithmic manipulation is proposed that distinguishes between loading and unloading paths. A representative approach is based on the comparison between the current separation and the maximum history separation (during the whole loading history from first load step till current one). The loading case is assumed when the current separation is the maximum one. In contrast, an unloading or reloading procedure is identified as long as the current separation is smaller than the maximum one, where the linear traction law is substituted. The maximum separation needs to be updated and saved as an internal variable at each loading step. Thereafter, the surface traction and the tangent quantities are rewritten as

$$\mathbf{t} = -\frac{\phi}{\Delta^2} \exp\left(-\frac{u_\Gamma^{max}}{\Delta}\right) \mathbf{u}_\Gamma \tag{11.57}$$

and

$$\mathfrak{k} = \begin{cases} \dfrac{\phi}{\Delta^2}\exp\left(-\dfrac{u_\Gamma^{\max}}{\Delta}\right)\mathbf{1} & \text{if } u_\Gamma^{\max} > \|\boldsymbol{u}_\Gamma\|, \\ \dfrac{\phi}{\Delta^2}\exp\left(-\dfrac{u_\Gamma^{\max}}{\Delta}\right)\left(\mathbf{1}-\dfrac{\boldsymbol{u}_\Gamma\otimes\boldsymbol{u}_\Gamma}{\Delta u_\Gamma^{\max}}\right) & \text{if } u_\Gamma^{\max} = \|\boldsymbol{u}_\Gamma\|, \end{cases} \tag{11.58}$$

respectively, by introducing the maximum separation

$$u_\Gamma^{\max} = \underset{\tau\leqslant t_{n+1}}{\mathrm{Max}} \|\boldsymbol{u}_\Gamma(\tau)\| = \underset{\tau\leqslant t_{n+1}}{\mathrm{Max}} \sqrt{\sum_{I=1}^{3}(l_c\,\Gamma^I)^2}. \tag{11.59}$$

Returning the quantities $\mathfrak{t}$ and $\mathfrak{k}$ to the RCE description, a consistent cohesive RCE phase-field modeling is obtained.

It is noteworthy that, in this example, the cohesive adhesion failure mechanism is formulated within a predefined phase-field crack path by setting the DIRICHLET boundary condition, which indicates that the crack orientation is also predefined in advance. As a result, the cohesive failure only occurs with respect to the existing phase-field crack path. Simultaneous evolution of crack propagation and cohesive adhesion failure at the evolved crack surfaces is not the scope of this work.

Inspired by Kim and Aragao (2013); Aragao (2011), which study a three-point bending test of a semi-circular specimen, the presented cohesive RCE phase-field approach is adopted for a numerical investigation. The experiment is shown in **Fig. 11.14** (a) and it is referred to Kim and Aragao (2013) for detailed insights. The specimen is a pre-notched semi-circular structure and it is characterized as bituminous mixture material. Two symmetrical points at the bottom edge are constrained along with the vertical direction and a downward displacement is applied at the top center of the curved boundary. Due to the symmetric properties of the geometry, the constraint and the loading condition, only half of the structure is taken into account for the numerical simulation, see **Fig. 11.14** (b). Since the cohesive crack path is known

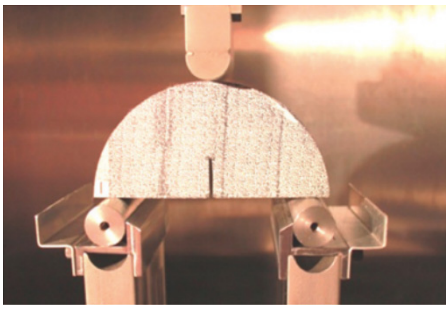

(a) experimental setup in Kim and Aragao (2013)

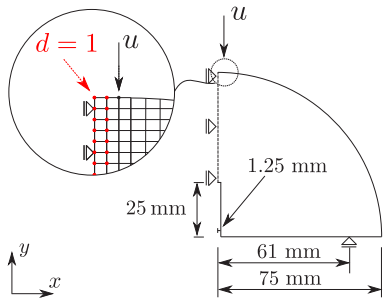

(b) simplified numerical model

Fig. 11.14: (a) Experimental setup according to Kim and Aragao (2013) and (b) corresponding geometrical setup for cohesive failure simulation for the SCB test.

as a fact according to the experimental validations in Kim and Aragao (2013); Aragao (2011), the present model is applied to study the cohesive behavior during the crack opening. The loading governed by displacement control is applied to a single node next to the crack path, see **Fig. 11.14** (b) for the numerical setup in detail.

According to a parametric calibration study, the material parameters are identified as λ=11.3 GPa, μ=26.5 GPa, T_{max}=19.2 kPa, ϕ=110 kN/m^2, l_c=1 mm and l=0.85 mm based on the experimental result in Aragao (2011). The relationship of the resultant load with respect to the crack mouth opening displacement (CMOD) shows good agreement with the data in Aragao (2011). As can be observed, the simulation successfully captures the gradual increase of reaction force at the initial loading phase (Phase I). After reaching the peak load (Phase II), the traction starts to decrease and the expected softening behavior (Phase III) is investigated. A slight difference exists for the final failure status (Phase IV), where the experimental result completely reduces the reaction force but the simulation does not yet.

Furthermore, **Fig. 11.15** shows the deformed shapes of the specimen at four representative phases, which are in accordance with **Fig. 11.16**. It is noteworthy that the rotation of the symmetric specimen results in a combination of a stiff contact in the vicinity top region of the cohesive zone and a tensile separation in the rest part. The aforementioned constrained minimization algorithm can appropriately address the issue and guarantee numerical robustness in such loading conditions. Another interesting investigation is the norm of the cohesive traction $\|\mathbf{t}\|$ in the cracked region, see **Figs. 11.17** (a)-(d) for Phase I-IV, respectively. For a straightforward un-

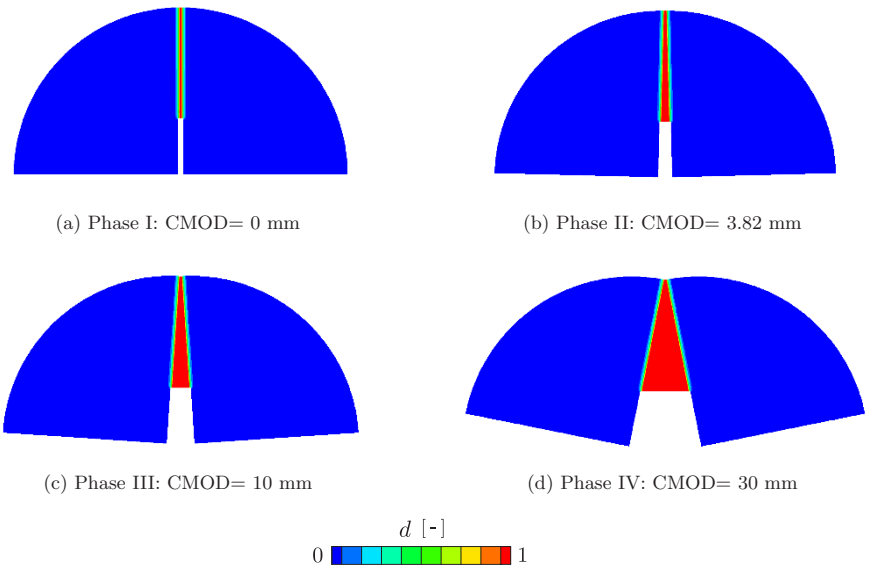

Fig. 11.15: Deformation of SCB specimen with a prescribed phase-field crack path using a mirroring post-processing technique.

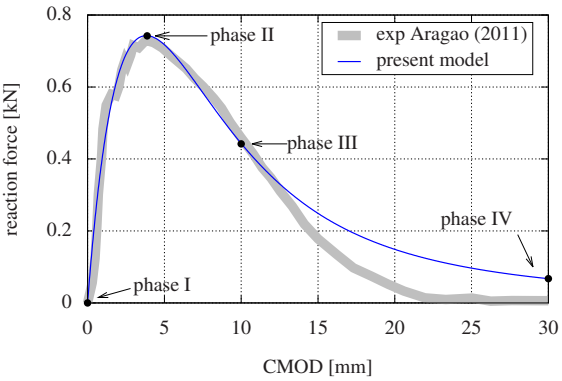

Fig. 11.16 Comparion of the load-CMOD relationships for the present simulation and the experimental prediction in Aragao (2011).

derstanding, the traction norm is plotted as outwards norm to the geometry plane and the height represents the magnitude of the traction norm. It can be easily seen that the traction norm evolves initially at the notch tip and 'propagates like a wave' from the notch tip towards the top of the specimen along the prescribed phase-field crack path. Eventually, **Fig. 11.17** (d) still shows a portion of cohesive tractions at the top region, which explains the reason why the reaction force in **Fig. 11.16** does not decrease to 0 at Phase IV. Using the same setup for the SCB test and model parameters, a further investigation with respect to different initial notch lengths is also included in this example. Three different initial lengths, i.e. $\mathrm{a} = [20, 25, 30]$ mm, are simulated, where the loading-CMOD relations are shown in **Fig. 11.18**. It can be found that the peak loads and the subsequent softening behavior are strongly affected by the initial notch length.

11.4.5 Contact Friction Modeling

Friction between crack faces is a well known property which influences crack propagation and the deformation of a fully evolved crack. However, friction is frequently neglected in models of phase-field fracture even in investigations on Mode II, Mode III and mixed mode deformations at the crack front. The influence of friction on brittle fracture is demonstrated in the following examples. Results are compared to the frictional phase-field approaches of Fei and Choo (2020a,b) and to discrete crack models considering friction.

Considering the present RCE framework, the traction term $\mathbf{t}$ is reformulated based on a classical COULOMB friction law. The friction force components for $\mathrm{I} = 2, 3$ are written as

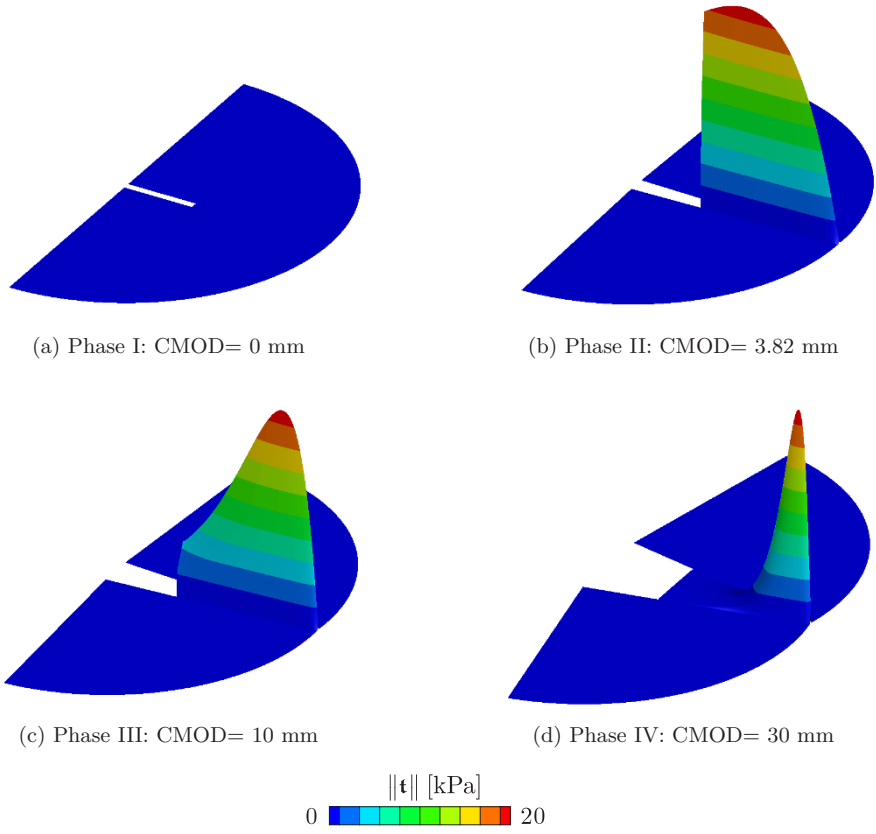

Fig. 11.17: Visualization of the cohesive traction norm $\|\mathfrak{t}\|$ along with the prescribed phase-field crack path by an out-plane description.

$$\begin{aligned}\mathfrak{t}^{\mathrm{I}} &= -\frac{1}{\mathcal{A}^{\Gamma}}\begin{cases}\mathfrak{f}^{\mathrm{I}}_{\mathrm{stat}}, & \text{for} \quad \|\mathbf{f}^{\mathrm{I}}_{\mathrm{stat}}\| \leqslant \|\mathbf{f}^{\mathrm{I}}_{\mathrm{dyna}}\|,\\ \mathfrak{f}^{\mathrm{I}}_{\mathrm{dyna}}, & \text{else},\end{cases}\\ \mathfrak{k}^{\mathrm{IJ}} &= \frac{1}{\mathcal{A}^{\Gamma}}\begin{cases}\mathsf{E}^{\Gamma}\delta_{\mathrm{IJ}}, & \text{for} \quad \|\mathbf{f}^{\mathrm{I}}_{\mathrm{stat}}\| \leqslant \|\mathbf{f}^{\mathrm{I}}_{\mathrm{dyna}}\|,\\ 0, & \text{else},\end{cases}\end{aligned} \tag{11.60}$$

where

$$\begin{cases}\mathfrak{f}^{\mathrm{I}}_{\mathrm{stat}} = -\mathsf{E}^{\Gamma}\left(\Gamma^{\mathrm{I}} - \Gamma^{\mathrm{I}}_{\mathrm{pl}}\right),\\ \mathfrak{f}^{\mathrm{I}}_{\mathrm{dyna}} = \mu\mathcal{A}^{\Gamma}\mathfrak{s} : \mathfrak{P}_{\mathrm{I}}\dfrac{\mathfrak{f}^{\mathrm{I}}_{\mathrm{stat}}}{\|\mathbf{f}^{\mathrm{I}}_{\mathrm{stat}}\|}.\end{cases}$$

The parameters μ and $\mathcal{A}^{\Gamma}$ are the friction coefficient and the crack surface area. Static friction (without surface sliding) is modeled via the penalty parameter E^{Γ}. The dynamic friction force $\mathbf{f}^{\mathrm{I}}_{\mathrm{dyna}}$ is proportional to the normal compression force, obtained from current stresses and the crack normal. Dynamic friction causes per-

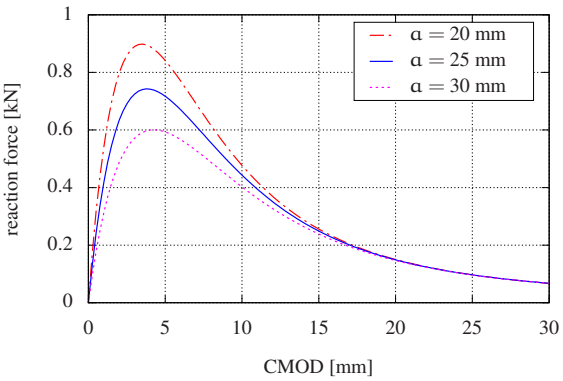

Fig. 11.18 Load-CMOD relationships evaluated at different lengths of the initial notch.

manent sliding deformation $\Gamma^{\mathrm{I}}_{\mathrm{pl}}$ between the crack surfaces. The crack state is considered for the evolution equation as

- opened crack, $\Gamma^{\mathrm{I}}_{\mathrm{pl},t_{n+1}} = \Gamma^{\mathrm{I}}_{t_n}$,
- closed crack and static friction, $\Gamma^{\mathrm{I}}_{\mathrm{pl},t_{n+1}} = \Gamma^{\mathrm{I}}_{\mathrm{pl},t_n}$,
- closed crack and dynamic friction, $\Gamma^{\mathrm{I}}_{\mathrm{pl},t_{n+1}} = \Gamma^{\mathrm{I}}_{t_n} + \dfrac{f^{\mathrm{I}}_{\mathrm{dyna}}}{E\Gamma}$.

It is notable that COULOMB's assumption of area independent friction forces is preserved in this model.

A long strip at compressive and shear loading is presented by Palmer et al. (1973), compare **Fig. 11.19**. The experiment is applied to over-consolidated clay observing significant cohesive fracture and crack surface friction. However, the experimental setup is adopted for the subsequent example and applied to brittle material behavior ($\mathcal{G}_c = 30$ J/mm) with COULOMB friction at the crack surfaces. The bulk material is considered as linear elastic ($E = 1$ GPa, $\nu = 0.3$) at small deformations. A fully constrained support is applied at the lower edge of the strip. The upper edge first undergoes a compressive displacement of $u_y = -0.01$ mm, followed by a tangential displacement of $u_x = 0.25$ mm applied in increments of $\Delta u_x = 0.25e-2$ mm. The model is uniformly discretized by 48400 linear elements.

The evolution of the phase-field is given in **Fig. 11.20** for different time steps and a friction coefficient of $\mu = 0.3$. The relations of the normal and tangential reaction

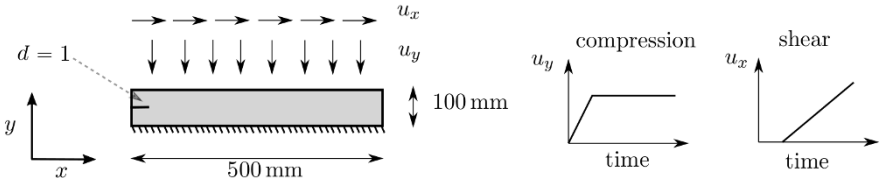

Fig. 11.19: Sketch of the long shear apparatus with initial phase-field crack and load history of normal and tangential displacement boundary conditions.

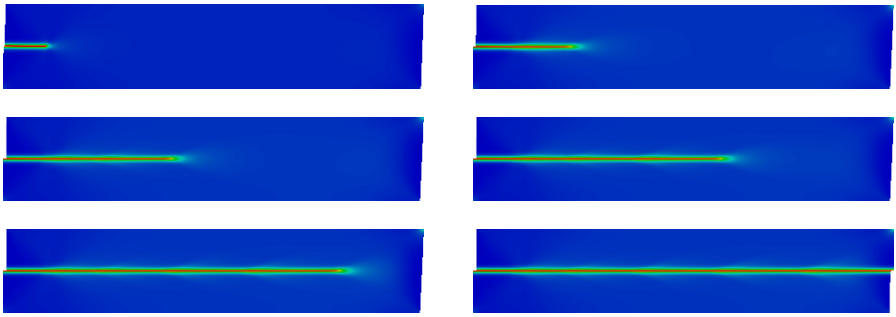

Fig. 11.20: Deformed shear strip with scaling factor 25 for different loading states, phase-field crack distribution during crack propagation.

forces versus tangential displacements are presented in **Fig. 11.21** for friction coefficients between $\mu = 0$ and $\mu = 1$. The comparison of the normal to the tangential reaction forces shows that the COULOMB law, which is applied at material level to the RCE model, is fulfilled at the component level, too. Furthermore, the initiation of crack propagation is significantly influenced by the frictional reaction force at the crack surface. The realistic relation between compression and friction force is also obtained by the cohesive phase-field model of Fei and Choo (2020b) considering crack friction. However, the approach presented there uses a directional decomposition of the stress based on the crack orientation but without considering lateral

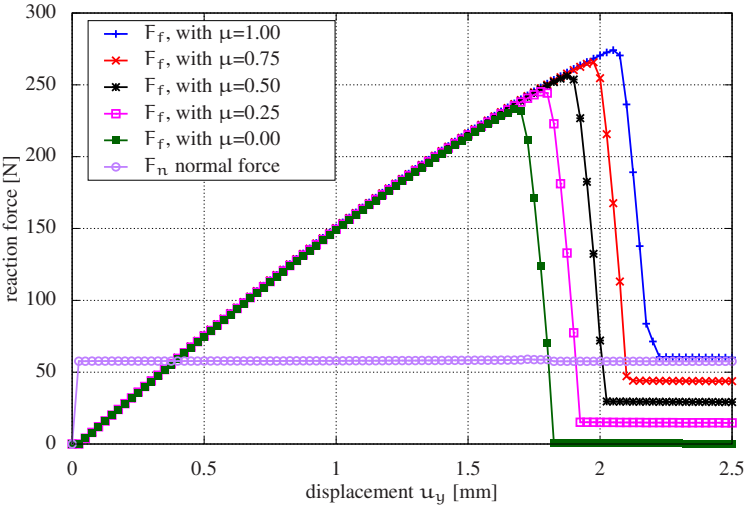

Fig. 11.21: Characteristics of normal force F_n versus tangential displacement and tangential frictional forces F_f for coefficients varied between $\mu = 0$ and $\mu = 1$.

contractions caused by POISSON's ratio ν. Additional criteria are introduced in order to distinguish frictional sticking and sliding. Crack surface contact is identified based on the sign of the normal strain which also misses lateral contractions at the crack surface. In contrast, the RCE framework allows for a realistic frictional crack model without the introduction of additional assumptions in order to approximate crack contact and frictional sticking.

11.5 Conclusions

Regularized formulations of the free discontinuity problem have been successfully applied to many classical and advanced problems of fracture mechanics in the past decade. A rapid development of phase-field fracture models could be observed, for instance, towards inelastic and anisotropic materials, fatigue behavior, multi-physical, multi-scale problems, frictional contact, and pore pressure models etc. Moreover, some fundamental challenges of classical fracture mechanical models, e.g., crack nucleation, crack branching, and proper discretizations, are solved by phase-field fracture and eigenfracture models. However, those models are recently shown to lack of reliable predictions for the crack contact state and the deformation kinematics at cracks. These intrinsic features of a fracture mechanical model are further related to the prediction of crack nucleation, propagation and branching. The recently introduced concept of representative crack elements provides a variational framework to couple physical crack models to regularized fracture formulations.

In this contribution, the fundamentals of representative crack elements are derived and the framework is presented in the context of phase-field fracture and eigenfracture. Discrepancies in previous models are demonstrated by consistency tests through a comparison to contact mechanical simulations. Same examples are further studied to verify deformation kinematics for cracks predicted by the models based on representative crack elements. The flexibility of the approach is finally proven by some applications to rate-dependent material, finite deformations, cohesive failure and crack surface friction.

References

Alessi R, Vidoli S, De Lorenzis L (2018) A phenomenological approach to fatigue with a variational phase-field model: The one-dimensional case. Engineering Fracture Mechanics 190:53–73, DOI 10.1016/j.engfracmech.2017.11.036

Alfano G, Crisfield MA (2001) Finite element interface models for the delamination analysis of laminated composites: mechanical and computational issues. International Journal for Numerical Methods in Engineering 50:1701–1736, DOI 10.1002/nme.93

Ambati M, Gerasimov T, De Lorenzis L (2015a) Phase-field modeling of ductile fracture. Computational Mechanics 55:1017–1040, DOI 10.1007/s00466-015-1151-4

Ambati M, Gerasimov T, De Lorenzis L (2015b) A review on phase-field models of brittle fracture and a new fast hybrid formulation. Computational Mechanics 55:383–405, DOI 10.1007/s00466-014-1109-y

Ambrosio L, Tortorelli VM (1990) Approximation of functional depending on jumps by elliptic functional via Γ-convergence. Communications on Pure and Applied Mathematics 43:999–1036, DOI 10.1002/cpa.3160430805

Ambrosio L, Fusco N, Pallara D (2000) Functions of Bounded Variation and Free Discontinuity Problems. Clarendon Press, Oxford

Amor H, Marigo JJ, Maurini C (2009) Regularized formulation of the variational brittle fracture with unilateral contact: Numerical experiments. Journal of the Mechanics and Physics of Solids 57:1209–1229, DOI 10.1016/j.jmps.2009.04.011

Aragao FTS (2011) Computational microstructure modeling of asphalt mixtures subjected to rate-dependent fracture. Ph.d. thesis, University of Nebraska-Lincoln

Barenblatt GI (1962) The mathematical theory of equilibrium cracks in brittle fracture. Advances in Applied Mechanics 7:55–129, DOI 10.1016/S0065-2156(08)70121-2

Blanco PJ, Sánchez PJ, Souza Neto EA, Feijóo RA (2016) Variational foundations and generalized unified theory of RVE-based multiscale models. Archives of Computational Methods in Engineering 23:191–253, DOI 10.1007/s11831-014-9137-5

Borden MJ, Hughes TJR, Landis CM, Verhoosel CV (2014) A higher-order phase-field model for brittle fracture: Formulation and analysis within the isogeometric analysis framework. Computer Methods in Applied Mechanics and Engineering 273:100–118, DOI 10.1016/j.cma.2014.01.016

Borden MJ, Hughes TJR, Landis CM, Anvari A, Lee IJ (2016) A phase-field formulation for fracture in ductile materials: Finite deformation balance law derivation, plastic degradation, and stress triaxiality effects. Computer Methods in Applied Mechanics and Engineering 312:130–166, DOI 10.1016/j.cma.2016.09.005

Bourdin B, Francfort GA, Marigo JJ (2000) Numerical experiments in revisited brittle fracture. Journal of the Mechanics and Physics of Solids 48:797–826, DOI 10.1016/S0022-5096(99)00028-9

Bourdin B, Francfort GA, Marigo JJ (2008) The variational approach to fracture. Journal of Elasticity 91:5–148

Braun M (1997) Configurational forces induced by finite-element discretization. Proceedings of the Estonian Academy of Sciences Physics - Mathematics 46:24–31

Bryant EC, Sun W (2018) A mixed-mode phase field fracture model in anisotropic rocks with consistent kinematics. Computer Methods in Applied Mechanics and Engineering 342:561–584, DOI 10.1016/j.cma.2018.08.008

Carrara P, Ambati M, Alessi R, De Lorenzis L (2020) A framework to model the fatigue behavior of brittle materials based on a variational phase-field approach. Computer Methods in Applied Mechanics and Engineering 361:112,731, DOI 10.1016/j.cma.2019.112731

Chambolle A, Conti S, Francfort GA (2018) Approximation of a brittle fracture energy with a constraint of non-interpenetration. Archive for Rational Mechanics and Analysis 228:867–889, DOI 10.1007/s00205-017-1207-z

De Giorgi E, Ambrosio L (1988) Un nuovo tipo di funzionale del calcolo delle variazioni. Atti della Accademia Nazionale dei Lincei Classe di Scienze Fisiche, Matematiche e Naturali Rendiconti Lincei Matematica e Applicazioni 82:199–210

Dugdale DS (1960) Yielding of steel sheets containing slits. Journal of the Mechanics and Physics of Solids 8:100–104, DOI 10.1016/0022-5096(60)90013-2

Fei F, Choo J (2020a) A phase-field method for modeling cracks with frictional contact. International Journal for Numerical Methods in Engineering 121:740–762, DOI 10.1002/nme.6242

Fei F, Choo J (2020b) A phase-field model of frictional shear fracture in geologic materials. Computer Methods in Applied Mechanics and Engineering 369:113,265, DOI 10.1016/j.cma.2020.113265

Foulk JW, Allen DH, Helms KLE (2000) Formulation of a three-dimensional cohesive zone model for application to a finite element algorithm. Computer Methods in Applied Mechanics and Engineering 183:51–66, DOI 10.1016/S0045-7825(99)00211-X

Francfort GA, Marigo JJ (1998) Revisiting brittle fracture as an energy minimization problem. Journal of the Mechanics and Physics of Solids 46:1319–1342, DOI 10.1016/S0022-5096(98)00034-9

Freddi F, Royer-Carfagni G (2009) Variational models for cleavage and shear fractures. Proceedings of the XIX AIMETA Symposium pp 715–716

Freddi F, Royer-Carfagni G (2010) Regularized variational theories of fracture: A unified approach. Journal of the Mechanics and Physics of Solids 58:1154–1174, DOI 10.1016/j.jmps.2010.02.010

Geelen RJM, Liu Y, Hu T, Tupek MR, Dolbow JE (2019) A phase-field formulation for dynamic cohesive fracture. Computer Methods in Applied Mechanics and Engineering 348:680–711, DOI 10.1016/j.cma.2019.01.026

Griffith AA (1921) The phenomena of rupture and flow in solids. Philosophical Transactions of the Royal Society of London Series A 221:163–198, DOI 10.1098/rsta.1921.0006

Gültekin O, Dal H, Holzapfel GA (2018) Numerical aspects of anisotropic failure in soft biological tissues favor energy-based criteria: A rate-dependent anisotropic crack phase-field model. Computer Methods in Applied Mechanics and Engineering 331:23–52, DOI 10.1016/j.cma.2017.11.008

Gurtin ME (2000) Configurational Forces as Basic Concepts of Continuum Physics. Applied Mathematical Sciences, Springer, New York, DOI 10.1007/978-0-387-22656-9_5

Hakim V, Karma A (2009) Laws of crack motion and phase-field models of fracture. Journal of the Mechanics and Physics of Solids 57:342–368, DOI 10.1016/j.jmps.2008.10.012

Henry H, Levine H (2004) Dynamic instabilities of fracture under biaxial strain using a phase field model. Physical Review Letters 93:105,504, DOI 10.1103/PhysRevLett.93.105504

Hesch C, Weinberg K (2014) Thermodynamically consistent algorithms for a finite-deformation phase-field approach to fracture. International Journal for Numerical Methods in Engineering 99:906–924, DOI 10.1002/nme.4709

Hill R (1963) Elastic properties of reinforced solids: Some theoretical principles. Journal of the Mechanics and Physics of Solids 11:357–372, DOI 10.1016/0022-5096(63)90036-X

Hocine N, Abdelaziz M, Imad A (2002) Fracture problems of rubbers : J integral estimation based upon η factors and investigation on the strain energy density distribution as a local criterion. International Journal of Fracture 117:1–23, DOI 10.1023/A:1020967429222

Kienzler R, Herrmann G (2000) Mechanics in Material Space: with Applications to Defect and Fracture Mechanics. Springer, Berlin, Heidelberg, DOI 10.1007/978-3-642-57010-0_4

Kim YR, Aragao FTS (2013) Microstructure modeling of rate-dependent fracture behavior in bituminous paving mixtures. Finite Elements in Analysis and Design 63:23–32, DOI 10.1016/j.finel.2012.08.004

Kuhn C, Müller R (2010) A continuum phase field model for fracture. Engineering Fracture Mechanics 77:3625–3634, DOI 10.1016/j.engfracmech.2010.08.009

Lancioni G, Royer-Carfagni G (2009) The variational approach to fracture mechanics. A practical application to the French Panthéon in Paris. Journal of Elasticity 95:1–30, DOI 10.1007/s10659-009-9189-1

Linse T, Hennig P, Kästner M, de Borst R (2017) A convergence study of phase-field models for brittle fracture. Engineering Fracture Mechanics 184:307–318, DOI 10.1016/j.engfracmech.2017.09.013

Loew PJ, Peters B, Beex LAA (2019) Rate-dependent phase-field damage modeling of rubber and its experimental parameter identification. Journal of the Mechanics and Physics of Solids 127:266–294, DOI 10.1016/j.jmps.2019.03.022

Luo C, Chen L, Huang Y (2021) A phase-field crack model based on a directional strain decomposition and a stress-driven Crack-Opening Indicator. Computer Methods in Applied Mechanics and Engineering 384:113,928, DOI 10.1016/j.cma.2021.113928

Mandal TK, Nguyen VP, Wu JY (2019) Length scale and mesh bias sensitivity of phase-field models for brittle and cohesive fracture. Engineering Fracture Mechanics 217:106,532, DOI 10.1016/j.engfracmech.2019.106532

Maugin GA (1995) Material forces: Concepts and applications. Applied Mechanics Reviews 48:213, DOI 10.1115/1.3005101

Maugin GA (2010) Configurational Forces: Thermomechanics, Physics, Mathematics, and Numerics. Routledge & CRC Press, Boca Raton

Miehe C, Gürses E (2007) A robust algorithm for configurational-force-driven brittle crack propagation with r-adaptive mesh alignment. International Journal for Numerical Methods in Engineering 72:127–155, DOI 10.1002/nme.1999

Miehe C, Schänzel LM (2014) Phase field modeling of fracture in rubbery polymers. Part I: Finite elasticity coupled with brittle failure. Journal of the Mechanics and Physics of Solids 65:93–113, DOI 10.1016/j.jmps.2013.06.007

Miehe C, Hofacker M, Welschinger F (2010a) A phase field model for rate-independent crack propagation: Robust algorithmic implementation based on operator splits. Computer Methods in Applied Mechanics and Engineering 199:2765–2778, DOI 10.1016/j.cma.2010.04.011

Miehe C, Welschinger F, Hofacker M (2010b) Thermodynamically consistent phase-field models of fracture: Variational principles and multi-field FE implementations. International Journal for Numerical Methods in Engineering 83:1273–1311, DOI 10.1002/nme.2861

Miehe C, Hofacker M, Schänzel LM, Aldakheel F (2015) Phase field modeling of fracture in multi-physics problems. Part II. Coupled brittle-to-ductile failure criteria and crack propagation in thermo-elastic-plastic solids. Computer Methods in Applied Mechanics and Engineering 294:486–522, DOI 10.1016/j.cma.2014.11.017

Mueller R, Maugin GA (2002) On material forces and finite element discretizations. Computational Mechanics 29:52–60, DOI 10.1007/s00466-002-0322-2

Nguyen VP, Wu JY (2018) Modeling dynamic fracture of solids with a phase-field regularized cohesive zone model. Computer Methods in Applied Mechanics and Engineering 340:1000–1022, DOI 10.1016/j.cma.2018.06.015

Ortiz M, Pandolfi A (1999) Finite-deformation irreversible cohesive elements for three-dimensional crack-propagation analysis. International Journal for Numerical Methods in Engineering 44:1267–1282

Özenç K, Kaliske M (2014) An implicit adaptive node-splitting algorithm to assess the failure mechanism of inelastic elastomeric continua. International Journal for Numerical Methods in Engineering 100:669–688, DOI 10.1002/nme.4774

Palmer AC, Rice JR, Hill R (1973) The growth of slip surfaces in the progressive failure of over-consolidated clay. Proceedings of the Royal Society of London A Mathematical and Physical Sciences 332:527–548, DOI 10.1098/rspa.1973.0040

Pandolfi A, Ortiz M (2012) An eigenerosion approach to brittle fracture. International Journal for Numerical Methods in Engineering 92:694–714, DOI 10.1002/nme.4352

Pandolfi A, Weinberg K, Ortiz M (2021) A comparative accuracy and convergence study of eigenerosion and phase-field models of fracture. Computer Methods in Applied Mechanics and Engineering 386:114,078, DOI 10.1016/j.cma.2021.114078

Pham K, Amor H, Marigo JJ, Maurini C (2011) Gradient damage models and their use to approximate brittle fracture. International Journal of Damage Mechanics 20:618–652, DOI 10.1177/1056789510386852

Qinami A, Pandolfi A, Kaliske M (2020) Variational eigenerosion for rate-dependent plasticity in concrete modeling at small strain. International Journal for Numerical Methods in Engineering 121:1388–1409, DOI 10.1002/nme.6271

Schänzel LM (2015) Phase field modeling of fracture in rubbery and glassy polymers at finite thermo-viscoelastic deformations. Phd thesis, Universität Stuttgart, Stuttgart

Schellekens JCJ, de Borst R (1993) On the numerical integration of interface elements. International Journal for Numerical Methods in Engineering 36:43–66, DOI 10.1002/nme.1620360104

Schmidt B, Fraternali F, Ortiz M (2009) An eigendeformation approach to variational fracture. Multiscale Modeling & Simulation 7(3):1237–1266, DOI 10.1137/080712568

Seiler M, Linse T, Hantschke P, Kästner M (2020) An efficient phase-field model for fatigue fracture in ductile materials. Engineering Fracture Mechanics 224:106,807, DOI 10.1016/j.engfracmech.2019.106807

Shen R, Waisman H, Guo L (2019) Fracture of viscoelastic solids modeled with a modified phase field method. Computer Methods in Applied Mechanics and Engineering 346:862–890, DOI 10.1016/j.cma.2018.09.018

Steinke C, Kaliske M (2019) A phase-field crack model based on directional stress decomposition. Computational Mechanics 63:1019–1046, DOI 10.1007/s00466-018-1635-0

Stochino F, Qinami A, Kaliske M (2017) Eigenerosion for static and dynamic brittle fracture. Engineering Fracture Mechanics 182:537–551, DOI 10.1016/j.engfracmech.2017.05.025

Storm J, Supriatna D, Kaliske M (2020) The concept of representative crack elements for phase-field fracture: Anisotropic elasticity and thermo-elasticity. International Journal for Numerical Methods in Engineering 121:779–805, DOI 10.1002/nme.6244

Storm J, Qinami A, Kaliske M (2021a) The concept of representative crack elements applied to eigenfracture. Mechanics Research Communications 116:103,747, DOI 10.1016/j.mechrescom.2021.103747

Storm J, Yin B, Kaliske M (2021b) The concept of representative crack elements (rce) for phase-field fracture - transient thermo-mechanics. submitted

Strobl M, Seelig T (2016) On constitutive assumptions in phase field approaches to brittle fracture. Procedia Structural Integrity 2:3705–3712, DOI 10.1016/j.prostr.2016.06.460

Teichtmeister S, Kienle D, Aldakheel F, Keip MA (2017) Phase field modeling of fracture in anisotropic brittle solids. International Journal of Non-Linear Mechanics 97:1–21, DOI 10.1016/j.ijnonlinmec.2017.06.018

van den Bosch MJ, Schreurs PJG, Geers MGD (2008) On the development of a 3D cohesive zone element in the presence of large deformations. Computational Mechanics 42:171–180, DOI 10.1007/s00466-007-0184-8

Verhoosel CV, de Borst R (2013) A phase-field model for cohesive fracture. International Journal for Numerical Methods in Engineering 96:43–62, DOI 10.1002/nme.4553

Vignollet J, May S, de Borst R, Verhoosel CV (2014) Phase-field models for brittle and cohesive fracture. Meccanica 49:2587–2601, DOI 10.1007/s11012-013-9862-0

Yin B, Kaliske M (2020a) An anisotropic phase-field model based on the equivalent crack surface energy density at finite strain. Computer Methods in Applied Mechanics and Engineering 369:113,202, DOI 10.1016/j.cma.2020.113202

Yin B, Kaliske M (2020b) A ductile phase-field model based on degrading the fracture toughness: Theory and implementation at small strain. Computer Methods in Applied Mechanics and Engineering 366:113,068, DOI 10.1016/j.cma.2020.113068

Yin B, Kaliske M (2020c) Fracture simulation of viscoelastic polymers by the phase-field method. Computational Mechanics 65:293–309, DOI 10.1007/s00466-019-01769-1

Yin B, Khodor J, Kaliske M (2020a) Fracture and fatigue failure simulation of polymeric material at finite deformation by the phase-field method and the material force approach. Advances in Polymer Science 286:347–376, DOI 10.1007/12_2020_63

Yin B, Steinke C, Kaliske M (2020b) Formulation and implementation of strain rate dependent fracture toughness in context of the phase-field method. International Journal for Numerical Methods in Engineering 121:233–255, DOI 10.1002/nme.6207

Yin B, Storm J, Kaliske M (2021) Viscoelastic phase-field fracture using the framework of representative crack elements. International Journal of Fracture DOI 10.1007/s10704-021-00522-1

Zhang X, Vignes C, Sloan SW, Sheng D (2017) Numerical evaluation of the phase-field model for brittle fracture with emphasis on the length scale. Computational Mechanics 59:737–752, DOI 10.1007/s00466-017-1373-8